Supporting Information of

Light and Copper-activated (Photo)cytotoxicity of 8-Hydroxyquinoline-based Boron Photosensitizers with Lipid Droplet Targeting and Lipid Peroxidation Accumulation

Thanh Chung Pham,[a+] Gun Kim,[b,+] Pham Van Thong,[c,d+] Tran Ngoc Dung,[c] Hung Tan Pham,[a] Nguyen Van Trang,[e] Le Thi Hong Hai,[c] Arne Meulemans,[a] Luc Van Meervelt,[a] Eduard Fron,[a] Mark Van der Auweraer,[a] Daniel Escudero,*[,a] Hue Minh Thi Nguyen,*[,c] Wim Dehaen*[,a]

[a]Department of Chemistry, KU Leuven, 3001 Leuven, Belgium

[b]Laboratory of Veterinary Pharmacology, College of Veterinary Science and Research Institute for Veterinary Science, Seoul National University, Seoul 08826, Korea

[c]Faculty of Chemistry and Center for Computational Science, Hanoi National University of Education, Hanoi, Vietnam

[d]R&DCenter, Vietnam Education and Technology Transfer JSC, Hanoi 100000, Vietnam

[e]Institute of Materials Science, Vietnam Academy of Science and Technology, 18 Hoang Quoc Viet, Cau Giay, Hanoi 10000, Viet Nam

Corresponding author:* daniel.escudero@kuleuven.be; hue.nguyen@hnue.edu.vn; wim.dehaen@kuleuven.be

[+]contribute equally

1. General and Materials.

All chemicals and materials mentioned on the synthesis procedure below were used without any further treatments. Triphenylborane (BPh_3), 8-hydroxyquinoline (QOH) and halogeno substituted derivatives (5-chloro/ClQOH, 5,7-dichloro/Cl_2QOH, 5,7-dibromo/Br_2QOH, 5,7-diiodo/I_2QOH, 5-chloro-7-iodo/IClQOH and 5,7-dichloro-2-methyl/$MeCl_2QOH$) were procured from Sigma–Aldrich. Metal ions used were stored as aqueous solutions of $MgCl_2$, $ZnCl_2$, $CdCl_2$, $CuCl_2$, $NiCl_2$, $CoCl_2$, $CrCl_3$, $AlCl_3$, $MnCl_2$, $FeCl_3$; $Pb(NO_3)_2$. The stock solutions of aforementioned were prepared in distilled water. Glass backed thin layer chromatography (TLC) plates, coated 0.25 mm silica gel 60 and indicator F254, were obtained from Merck. All TLC experiments were visualized under UV-light at 254 nm. UV-Vis absorption spectra were recorded on a PerkinElmer Lambda 40 spectrophotometer using blank correction. Fluorescence spectra were recorded on a HORIBA Jobin Yvon Fluorolog FL3-22 fluorimeter and corrections for the excitation beam intensity, the wavelength dependent sensitivity of the detector and the optical path were applied. The infrared spectra were recorded on IMPACK-410 NICOLET spectrometer in KBr discs in the range 4000–400 cm^{-1}. Mass spectra were measured using a UPLC-MS spectrometer (Waters). The ^1H NMR measurements were conducted on a Bruker AVANCE 500 MHz at 298–300 K using TMS as the internal chemical shift reference. The abbreviations are used to designated the multiplicities: s = singlet, d = doublet, dd = doublet of doublets, t = triplet, m = multiplet.

2. Synthetic process

A mixture of triphenylborane (121 mg, 0.5 mmol) and 8-hydroxyquinoline derivatives (RQOH/0.5 mmol) in 15 mL chloroform was stirred at ambient temperature (AT) and filtered after 30 minutes to eliminate the insoluble part. Then, the resulting clear solution evaporated slowly at AT within 24 h afforded the products **BQ1–BQ7** as greenish-yellow crystals, of which the single crystals of **BQ2**, **BQ6** and **BQ7** were suitable for X-ray diffraction analysis.

The complexes were obtained as green crystalline solids with a high yield of 85-95%. They exhibit excellent stability towards air and moisture and have slight solubility in water while being soluble in certain organic solvents, particularly halogenated solvents like $CHCl_3$ and CH_2Cl_2. The structures of the new complexes including **BQ2**, **BQ3** and **BQ5–BQ7**, have been characterized by ESI mass spectrometry, IR and ^1H NMR spectroscopy. In the positive-mode ESI mass spectra of all complexes, the $[M + Na]^+$ ions are observed with intensity of 25-100%, which provides evidence for the proposed RQO coordination. In the IR spectra there is no evidence for a νOH band, indicating that the RQOH have been deprotonated to form a bidentate ligand and are chelated with B(III) through the N and O atoms. Furthermore, the data of the ^1H NMR spectra of all complexes (see experimental) show the presence of the phenyl groups and the RQO in a 2:1 ratio, which shows good agreement with the results obtained from ESI mass spectrometry. In particular, the absence of a proton of the phenol OH group again confirms the chelating coordination of RQO with B(III).

BQ1: Yield: 139 mg (90%). ^1H NMR (600 MHz, chloroform-d_1): δ 8.57 (dd, ^3J(H,H) = 5.0 Hz, ^4J(H,H) = 1.0 Hz, 1H, Ar−H), 8.39 (d, ^3J(H,H) = 8.5 Hz, 1H, Ar−H), 7.65 (t, ^3J(H,H) = 8.5 Hz, 1H, Ar−H), 7.60 (dd, ^3J(H,H) = 5.0 Hz, 8.5 Hz, 1H, Ar−H), 7.45 (dd, ^3J(H,H) = 8.0 Hz, ^4J(H,H) = 1.0 Hz, 4H, Ar−H), 7.28−7.25 (m, 4H, Ar−H), 7.24−7.21 (m, 3H, Ar−H), 7.17 (d, ^3J(H,H) = 8.5 Hz, 1H, Ar−H). ^{13}C NMR (151 MHz, $CDCl_3$) δ 158.81, 139.31, 138.75, 137.63, 132.94, 132.02, 128.48, 127.62, 127.01, 122.78, 112.23, 109.75. FT-IR (cm^{-1}): 3068 (CH), 1612, 1578 (C=C). Elemental analysis for $C_{21}H_{16}BNO$: Calcd. C 81.55, H 5.18, N 4.53; Found C 81.64, H 5.25, N 4.36. (MAD = 0.11)

BQ2: Yield: 146 mg (85%). ^{1}H NMR (600 MHz, chloroform-d_1): δ 8.64 (d, ^3J(H,H) = 8.5 Hz, 1H, Ar–H), 8.63 (d, ^3J(H,H) = 5.0 Hz, 1H, Ar–H), 7.73 (dd, ^3J(H,H) = 5.0 Hz, 8.5 Hz, 1H, Ar–H), 7.68 (d, ^3J(H,H) = 8.0 Hz, 1H, Ar–H), 7.44 (d, ^3J(H,H) = 8.0 Hz, 4H, Ar–H), 7.29–7.23 (m, 6H, Ar–H), 7.10 (d, ^3J(H,H) = 8.0 Hz, 1H, Ar–H). ^{13}C NMR (101 MHz, $CDCl_3$) δ 157.92, 140.11, 138.05, 136.61, 132.25, 131.97, 127.72, 127.22, 126.50, 123.55, 115.39, 109.88. MS (ESI) Calcd for $[M + Na]^+$, $BC_{21}H_{15}NOCl$: *m/z* 366. Found (%): *m/z* 366 (40). FT-IR (υ, cm^{-1}): 3055, 3008 (CH), 1610, 1578, 1503 (C=C). : Elemental analysis for $C_{21}H_{15}BClNO$: Calcd. C 73.36, H 4.37, N 4.08; Found C 73.58, H 4.68, N 4.16 (MAD = 0.20).

BQ3: Yield: 174 mg (92%). ^{1}H NMR (600 MHz, chloroform-d_1): δ 8.67 (d, ^3J(H,H) = 5.0 Hz, 1H, Ar–H), 8.64 (d, ^3J(H,H) = 8.5 Hz, 1H, Ar–H), 7.75 (dd, ^3J(H,H) = 5.0 Hz, 8.5 Hz, 1H, Ar–H), 7.74 (s, 1H, Ar–H), 7.44 (dd, ^3J(H,H) = 8.5 Hz, ^4J(H,H) = 1.5 Hz, 4H, Ar–H), 7.29–7.26 (m, 4H, Ar–H), 7.25–7.23 (m, 2H, Ar–H). ^{13}C NMR (151 MHz, $CDCl_3$) δ 153.90, 141.08, 137.83, 136.94, 132.67, 131.99, 127.72, 127.35, 125.23, 123.37, 115.98, 114.48. MS (ESI) Calcd for $[M + Na]^+$, $BC_{21}H_{14}NOCl_2Na$: *m/z* 400. Found (%): *m/z* 400 (25). FT-IR (υ, cm^{-1}): 3055, 3014 (CH), 1608, 1578, 1499 (C=C). Elemental analysis for $C_{21}H_{14}BCl_2NO$: Calcd. C 66.67, H 3.70, N 3.70; Found C 66.42, H 3.78, N 3.62 (MAD = 0.14).

BQ4: Yield: 205 mg (88%). ^{1}H NMR (600 MHz, chloroform-d_1): δ 8.64 (d, ^3J(H,H) = 5.0 Hz, 1H, Ar–H), 8.58 (d, ^3J(H,H) = 8.5 Hz, 1H, Ar–H), 8.03 (s, 1H, Ar–H), 7.74 (dd, ^3J(H,H) = 5.0 Hz, 8.5 Hz, 1H, Ar–H), 7.43 (dd, ^3J(H,H) = 8.0 Hz, ^4J(H,H) = 1.0 Hz, 4H, Ar–H), 7.29–7.27 (m, 4H, Ar–H), 7.25–7.24 (m, 2H, Ar–H). ^{13}C NMR (101 MHz, $CDCl_3$) δ 140.98, 139.10, 137.91, 132.00, 127.71, 127.34, 126.97, 123.66, 103.96, 102.58. FT-IR (υ, cm^{-1}): 3049 (CH), 1598, 1573 (C=C). Elemental analysis for $C_{21}H_{14}BBr_2NO$: Calcd. C 53.96, H 3.0, N 3.0; Found C 53.72, H 3.08, N 2.96 (MAD = 0.12).

BQ5: Yield: 244 mg (87%). ^{1}H NMR (600 MHz, chloroform-d_1): δ 8.59 (dd, ^3J(H,H) = 5.0 Hz, ^4J(H,H) = 1.0 Hz, 1H, Ar–H), 8.42 (dd, ^3J(H,H) = 8.5 Hz, ^4J(H,H) = 1.0 Hz, 1H, Ar–H), 7.99 (s, 1H, Ar–H), 7.72 (dd, ^3J(H,H) = 5.0 Hz, 8.5 Hz, 1H, Ar–H), 7.43 (dd, ^3J(H,H) = 8.0 Hz, ^4J(H,H) = 1.0 Hz, 4H, Ar–H), 7.29–7.26 (m, 4H, Ar–H), 7.25–7.23 (m, 2H, Ar–H). MS (ESI) Calcd for $[M + Na]^+$, $BC_{21}H_{14}NOI_2Na$: *m/z* 584. Found (%): *m/z* 584 (100). FT-IR (υ, cm^{-1}): 3045, 3008 (CH), 1601, 1588, 1569 (C=C). Elemental analysis for $C_{21}H_{14}BI_2NO$: Calcd. C 45.0, H 2.50, N 2.50; Found C 44.95, H 2.71, N 2.48 (MAD = 0.09).

BQ6: Yield: 211 mg (90%). ^{1}H NMR (600 MHz, chloroform-d_1): δ 8.64 (d, ^3J(H,H) = 5.0 Hz, 1H, Ar–H), 8.62 (d, ^3J(H,H) = 8.5 Hz, 1H, Ar–H), 7.99 (s, 1H, Ar–H), 7.74 (dd, ^3J(H,H) = 5.0 Hz, 8.5 Hz, 1H, Ar–H), 7.44 (d, ^3J(H,H) = 8.5 Hz, ^4J(H,H) = 1.0 Hz, 4H, Ar–H), 7.29–7.24 (m, 6H, Ar–H). ^{13}C NMR (101 MHz, $CDCl_3$) δ 159.26, 140.90, 139.28, 136.99, 135.52, 132.01, 127.71, 127.31, 127.20, 126.20, 123.57, 116.19. MS (ESI) Calcd for $[M + Na]^+$, $BC_{21}H_{14}NOIClNa$: *m/z* 492. Found (%): *m/z* 492 (50). FT-IR (υ, cm^{-1}): 3065, 3047, 3008 (CH), 1610, 1595, 1570 (C=C). Found C 53.48, H 3.16, N 3.21 (MAD = 0.21).

BQ7: Yield: 186 mg (95%). ^{1}H NMR (600 MHz, chloroform-d_1): δ 8.53 (d, ^3J(H,H) = 8.0 Hz, 1H, Ar–H), 7.65 (s, 1H, Ar–H), 7.48 (d, ^3J(H,H) = 8.0 Hz, 1H, Ar–H), 7.37 (dd, ^3J(H,H) = 8.5 Hz, ^4J(H,H)

= 1.5 Hz, 4H, Ar−H), 7.29–7.24 (m, 6H, Ar−H), 2.57 (s, 3H, CH_3). ^{13}C NMR (101 MHz, $CDCl_3$) δ 155.52, 153.69, 138.07, 136.84, 133.33, 131.39, 127.58, 127.30, 125.86, 123.52, 115.85, 114.27, 21.55. MS (ESI) Calcd for $[M + Na]^+$, $BC_{22}H_{16}NOCl_2Na$: *m/z* 414. Found (%): *m/z* 414 (100). FT-IR (υ, cm^{-1}): 3071 (CH), 1608, 1578, 1499 (C=C). Elemental analysis for $C_{22}H_{16}BCl_2NO$: Calcd. C 67.35, H 4.08, N 3.57; Found C 67.72, H 4.39, N 3.59 (MAD = 0.23).

3. Crystallographic Measurements. X-ray intensity data for **BQ2** and **BQ6** were collected at 293(2) K on an Agilent SuperNova diffractometer, equipped with an Eos CCD detector, using MoKα radiation (λ = 0.71073 Å). The images were interpreted and processed with the CrysAlisPro software from Agilent Technologies. Using Olex2, the structures were solved with the ShelXT structure solution program using Intrinsic Phasing and refined with the ShelXL refinement package using full-matrix least squares minimization on F^2. Intensities for the X-ray determination of **BQ7** were collected on a Bruker D8 Quest instrument at 273(2) K with Mo Kα radiation (λ = 0.71073 Å) using a TRIUMPH monochromator. Standard procedures were applied for data reduction and absorption correction. Using Olex2, the structure was solved with the olex2.solve structure solution program using Charge Flipping and refined with the ShelXL [D] refinement package using full-matrix least squares minimization on F^2. Non-hydrogen atoms were refined anisotropically. All H-atoms were included in calculated positions and treated as the riding atoms with C-H = 0.93 (aromatic H) and 0.96 (methyl group) Å and with isotropic temperature factors fixed at 1.2 times U_{eq} of the parent atoms (1.5 for methyl group). A summary of the crystal data for **BQ2**, **BQ6** and **BQ7** is given in **Table S2**. Crystal structure validations and geometrical calculations were performed using the Platon software [31]. Crystallographic data for the structures reported herein have been deposited with the Cambridge Crystallographic Data Centre as supplementary publication numbers CCDC 2247826-2247828. The data can be obtained free of charge via http://www.ccdc.cam.ac.uk/conts/retrieving.html, or from the Cambridge Crystallographic Data Center, 12 Union Road, Cambridge CB2 1EZ, UK; fax: +441223 336 033; or e-mail: deposit@ccdc.cam.ac.uk

Table S1. Selected bond parameters of complexes of **BQ2**, **BQ6** and **BQ7**[a]

	B–C	B–N	B–O	C–B–C	C–B–O	O–B–N	C–B–N
BQ2	1.607(3) 1.612(3)	1.641(3)	1.537(2)	117.89(17)	110.53(16) 110.20(17)	97.94(14)	107.58(16) 110.84(15)
BQ6	1.600(4) 1.605(4)	1.635(4)	1.545(4)	117.4(2)	108.3(2) 111.6(2)	98.21(19)	108.4(2) 111.4(2)
BQ7	1.598(3) 1.616(4)	1.490(4)	1.533(3)	117.7(2)	109.44(19) 110.30(19)	97.86(17)	108.21(19) 111.52(19)

[a] Bond lengths (Å) and angles (°).

BQ2 crystallizes in the monoclinic space group $P2_1/c$. The planar quinoline ring (r.m.s. deviation = 0.004 Å) makes an angle of 80.27(8)° and 74.51(9)° with phenyl rings C10-C15 and C16-C21, respectively. The substituents of the quinoline ring are coplanar with deviations from the mean plane through the quinoline ring being -0.015(1) Å for O1 and -0.007(1) Å for Cl1, and atom B1 showing the highest deviation of -0.067 (2) Å. Due to the orientation of the C10-C15 ring a short H11···O1 interaction is possible (2.57 Å). The crystal packing of **BQ2** exhibits C-H···π and partial π···π interactions as illustrated in **Figure 1a** [H6···*Cg*4^{i} = 2.77 Å, *Cg*2···*Cg*2^{i} = 3.9712(12) Å, slippage 2.077 Å, *Cg*2 and *Cg*4 are the centroids of rings N1/C5-C9 and C10-C15, respectively, symmetry code: (i) 1-*x*, 1-*y*, 1-*z*]. Compound **BQ6** crystallizes in the monoclinic space group $P2_1/n$. The quinoline ring is less planar (r.m.s. deviation = 0.024 Å) and makes an angle of 73.08(13)° and 81.04(13)° with phenyl rings C10-C15 and C16-C21, respectively. The I1 substituent deviates most from the quinoline plane (0.109 Å), followed by Cl1 (-0.091 Å), O1 (0.082 Å) and B1 (-0.048 Å). Several C-H···π interactions are observed in the crystal packing of **BQ6**: H3···*Cg*4^{i} (3.00 Å), H6···*Cg*5^{ii} (2.79 Å), and H12···*Cg*5^{iii} (2.95 Å) [**Figure 1b**, Cg4 and Cg5 are the centroids of rings C10-C15 and C16-C21, respectively, symmetry codes: (i), (ii), (iii)]. Compound **BQ7** crystallizes in the orthorhombic space group *Pbca*. The planar quinoline ring (r.m.s. deviation = 0.006 Å) makes an angle of 78.63(10)° and 74.14(9)° with phenyl rings C10-C15 and C16-C21, respectively. Deviations from the mean plane through the quinoline ring are 0.015(2) Å for O1, 0.008(1) Å for Cl1, -0.018(1) Å for Cl2 and the highest deviation of -0.061 (2) Å for B1. A short intramolecular H15···O1 interaction is observed (2.50 Å). The crystal packing of **BQ7** is characterized by C-H…π interactions [**Figure 1c**, H7…*Cg*4^{i} = 2.74 Å, H21…*Cg*4^{ii} = 2.98 Å, *Cg*4 is the centroid of the C10-C15 ring, symmetry codes: (i) -1/2+*x*, *y*, 3/2-*z*, (ii) 1-*x*, 1/2+*y*, 3/2-*z*].

4. Photophysical characteristics

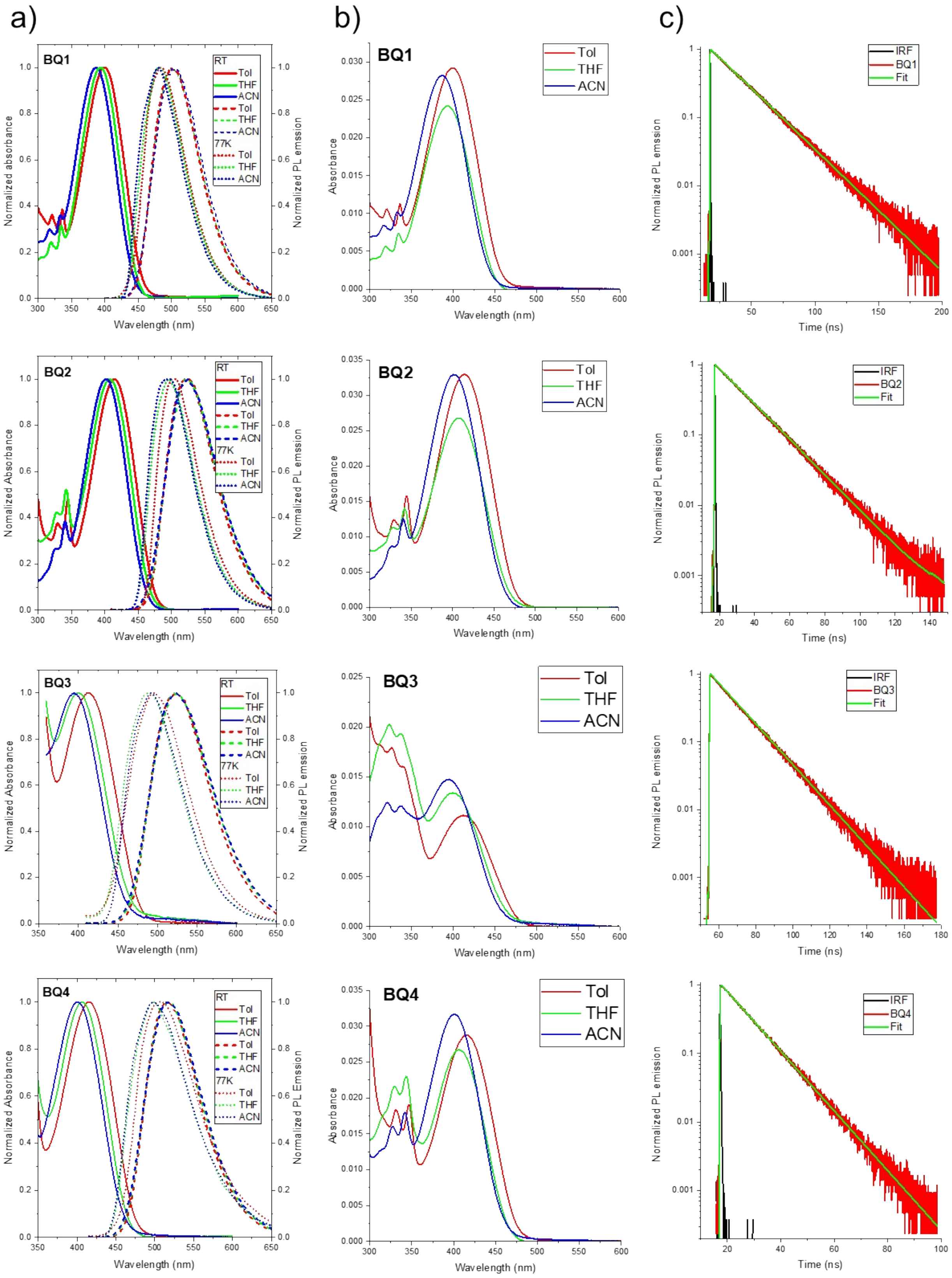

Figure S1. a) Normalized UV-Vis absorption (solid line) and PL emissions spectra (dash line, RT; dot line, 77K) of **BQ1-BQ4** ; b) UV-Vis absorption spectra of **BQ1-BQ4** at in solvents at RT (10 μM, λ_{ex} = 390 nm); c) Fluorescence decay trace of **BQ1-BQ4** in toluene (λ_{ex} = 400 nm).

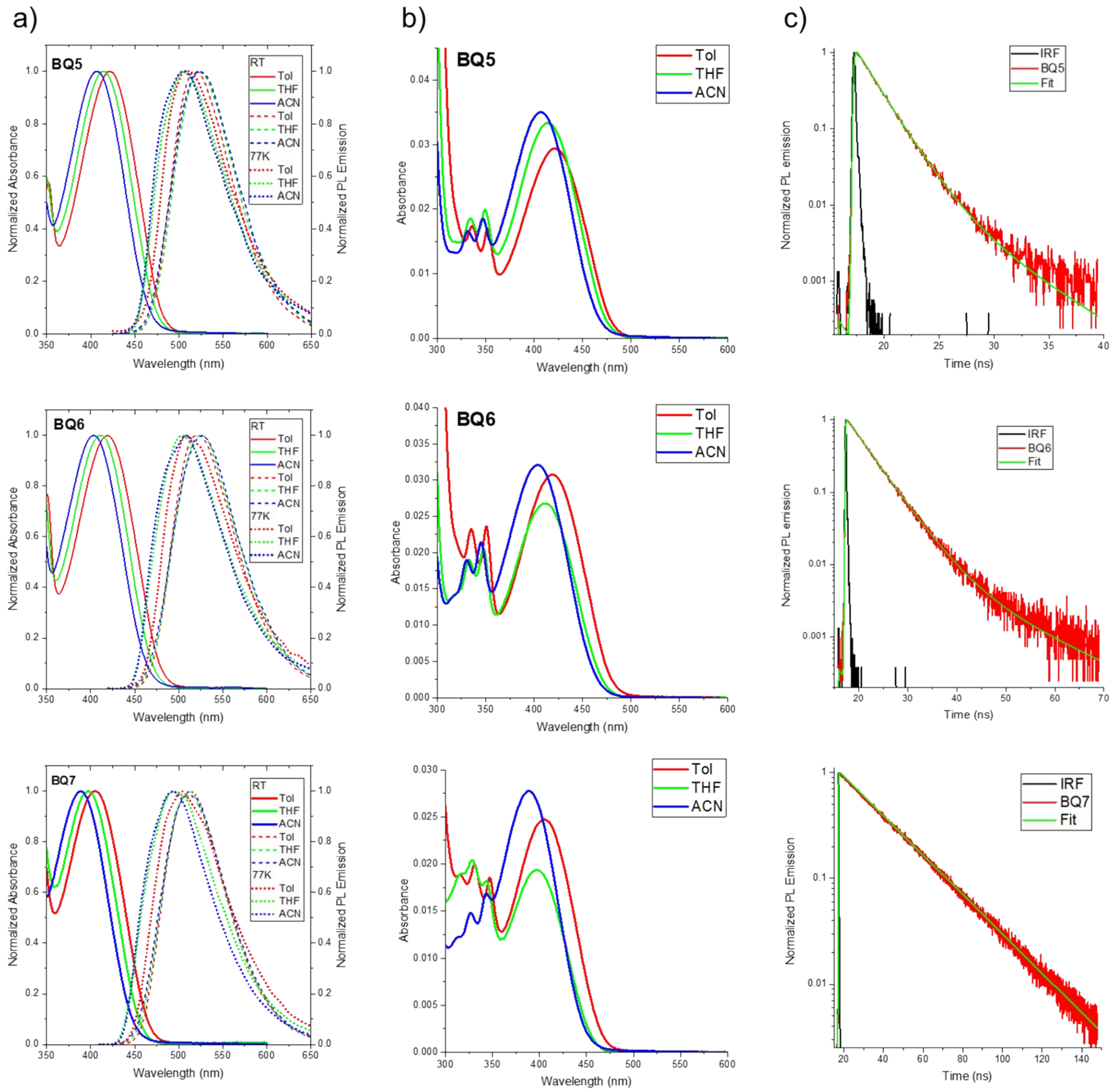

Figure S2. a) Normalized UV-Vis absorption (solid line) and PL emissions spectra (dash line, RT; dot line, 77K) of **BQ5-BQ7** (10 μM, λ_{ex} = 390 nm); b) UV-Vis absorption spectra of **BQ5-BQ7** at in solvents at RT (10 μM, λ_{ex} = 390 nm); c) Fluorescence decay trace of **BQ5-BQ7** in toluene (λ_{ex} = 400 nm).

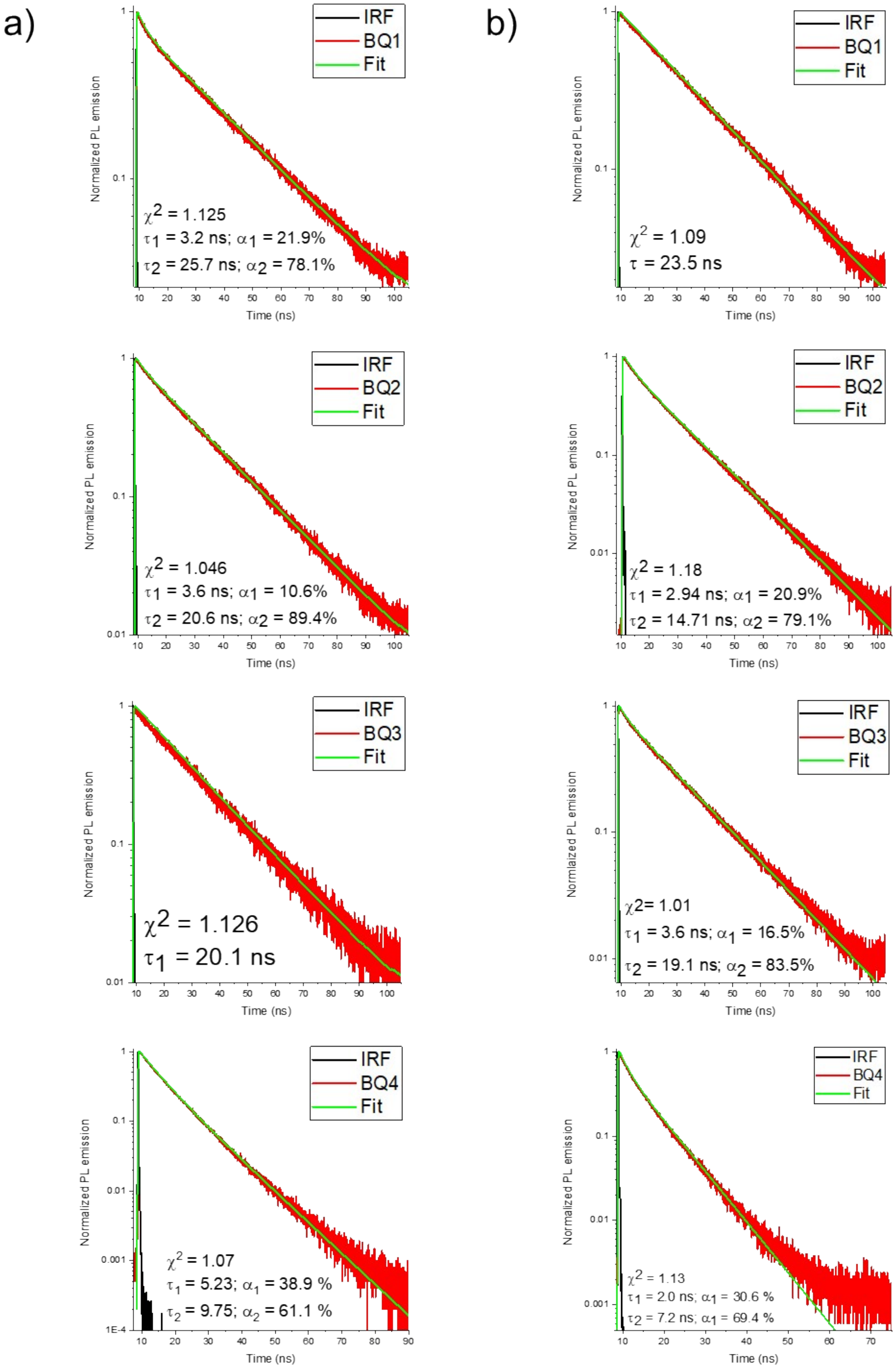

Figure S3. Fluorescence decay trace of **BQ1-BQ4** in a) Film and b) Solid (λ_{ex} = 400 nm).

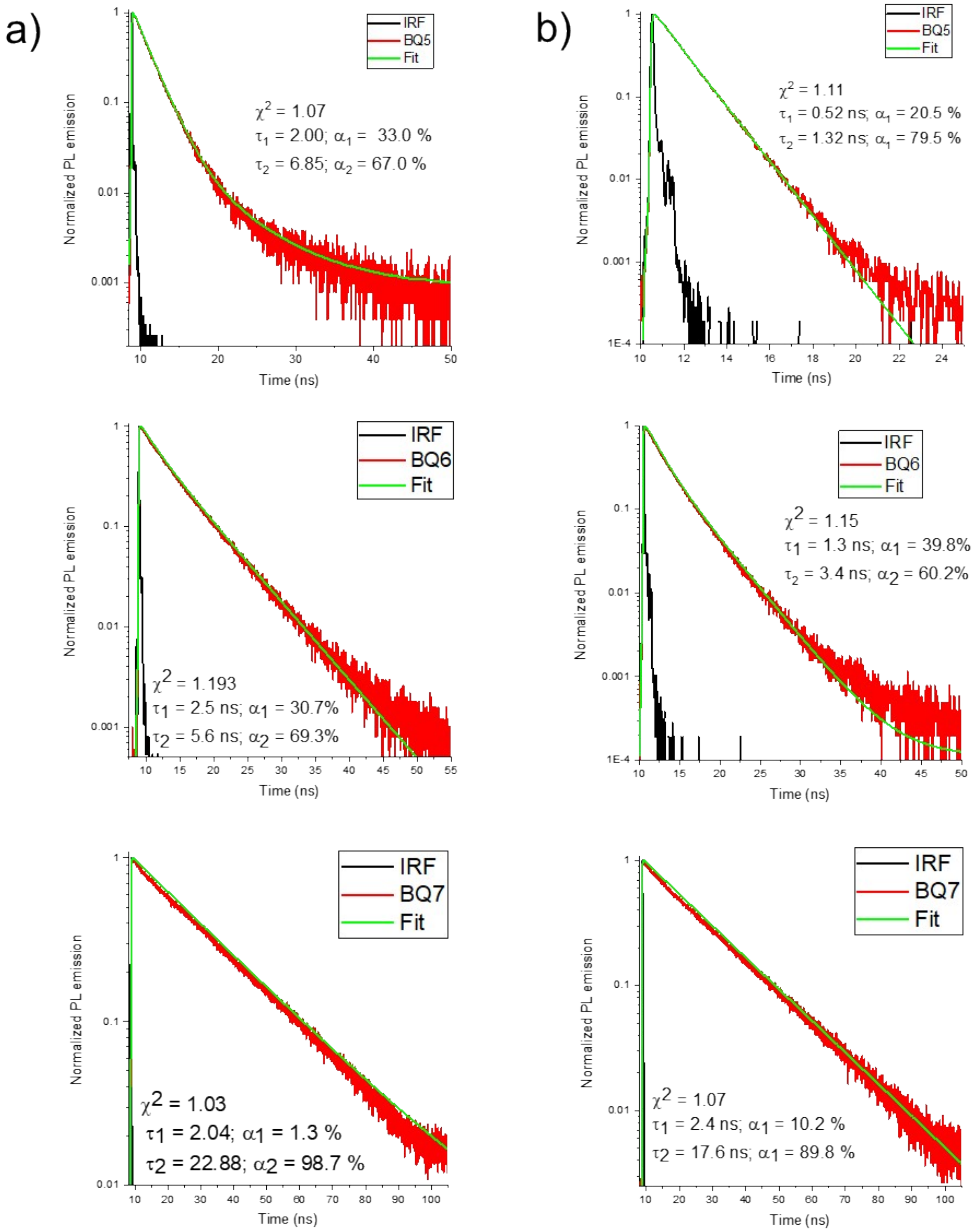

Figure S4. Fluorescence decay trace of **BQ5-BQ7** in a) Film and b) Solid (λ_{ex} = 400 nm).

Table S2. Fluorescence lifetime (τ) and amplitude (α) of **BQ1-BQ7** in film and solid state.

	Film		Solid	
	τ_1 (ns)/α_1 (%)	τ_2 (ns)/α_2 (%)	τ_1 (ns)/α_1 (%)	τ_2 (ns)/α_2 (%)
BQ1	3.2/21.9	25.7/78.1	23.5/100	-
BQ2	3.6/10.6	20.6/89.4	2.9/20.9	14.7/79.1
BQ3	20.1/100	-	3.6/16.5	19.1/83.5
BQ4	5.23/38.9	9.75/61.1	2.0/30.6	7.2/69.4
BQ5	2.00/33.0	6.85/67.0	0.5/20.5	1.32/79.5
BQ6	2.5/30.7	5.6/69.3	1.3/39.8	3.4/60.2
BQ7	2.04/1.3	22.9/98.7	2.4/10.2	17.6/89.8

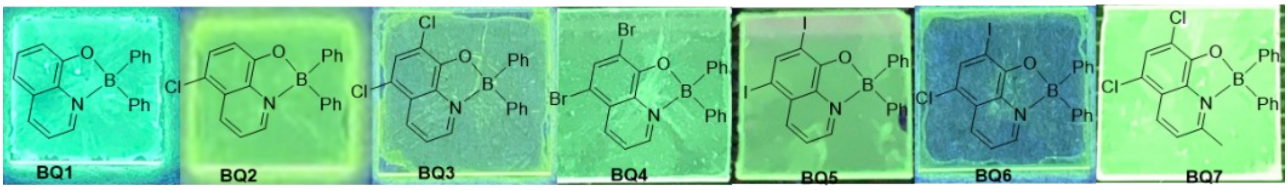

Figure S5. Fluorescence emission image of **BQ1** – **BQ7** in Zoenex film under 365 nm light.

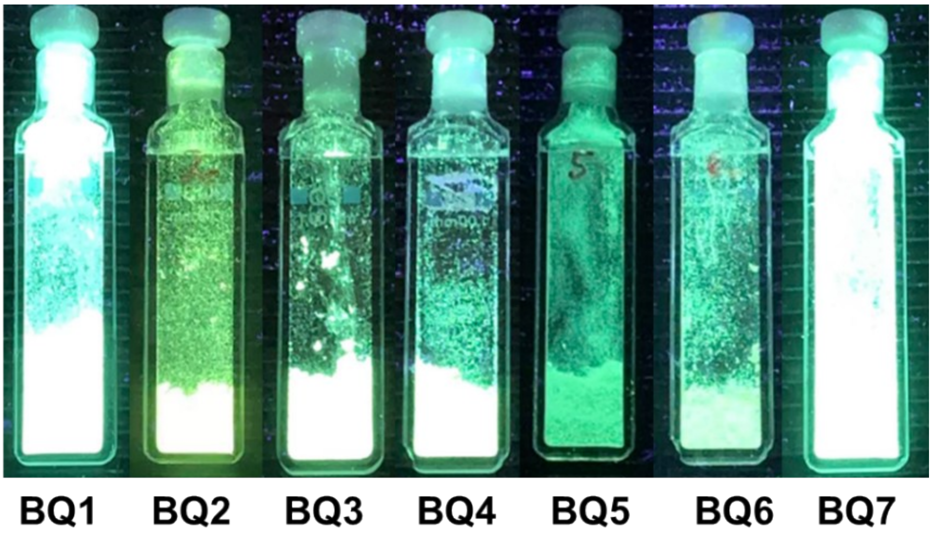

Figure S6. Fluorescence emission image of **BQ1** – **BQ7** in solid state under 365 nm light.

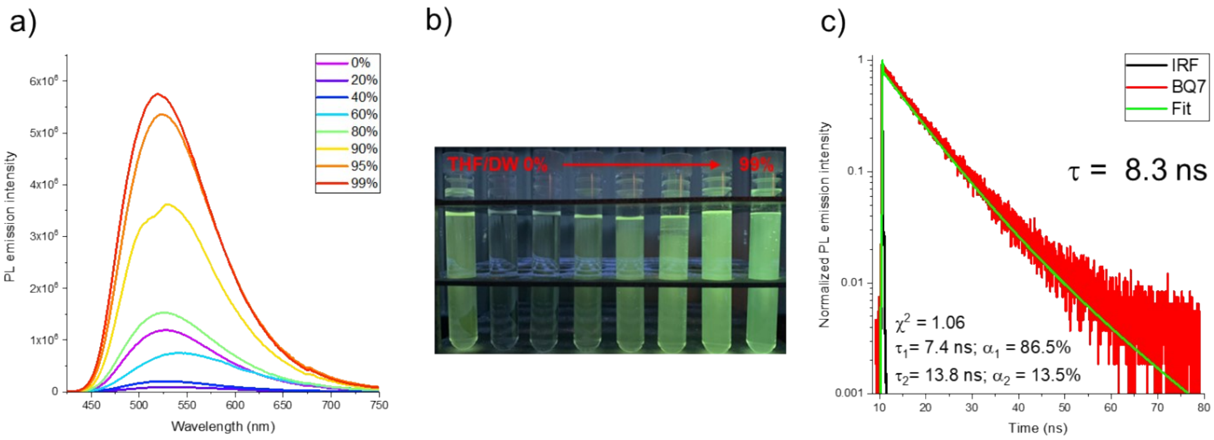

Figure S7. Fluorescence emission spectra (a) and image (b) of **BQ7** (10 μM) in THF/DW (0 - 99%); c) Fluorescence decay trace of **BQ7** (10 μM) in THF/DW (5/95).

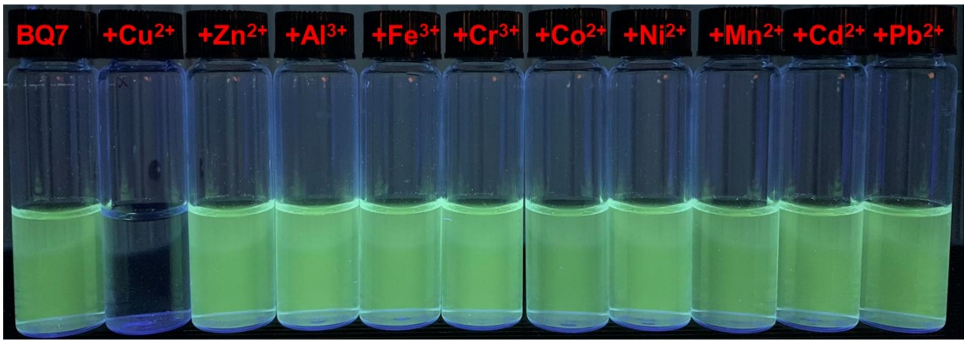

Figure S8. Fluorescence image of **BQ7** (10 μM) in the presence of metal cation (10.0 eq) in THF/DW (5/95)

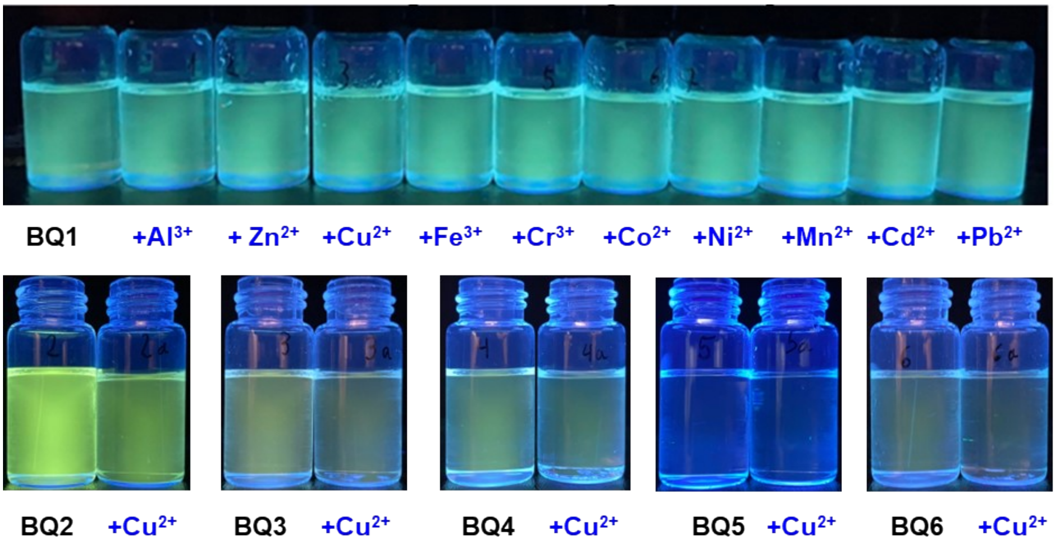

Figure S9. Fluorescence image of **BQ1** (10 μM) with various cation (10.0 eq) and **BQ2-BQ6** (10 μM) with Cu^{2+} cation (10.0 eq) in THF/DW (5/95).

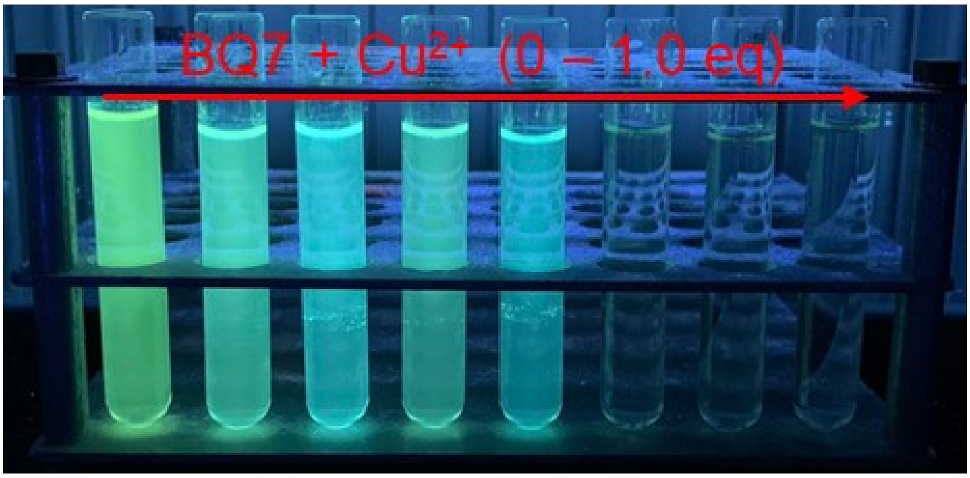

Figure S10. Fluorescence image of **BQ7** (10 μM) in the presence of Cu^{2+} (0 - 1.0 eq) in THF/DW (5/95)

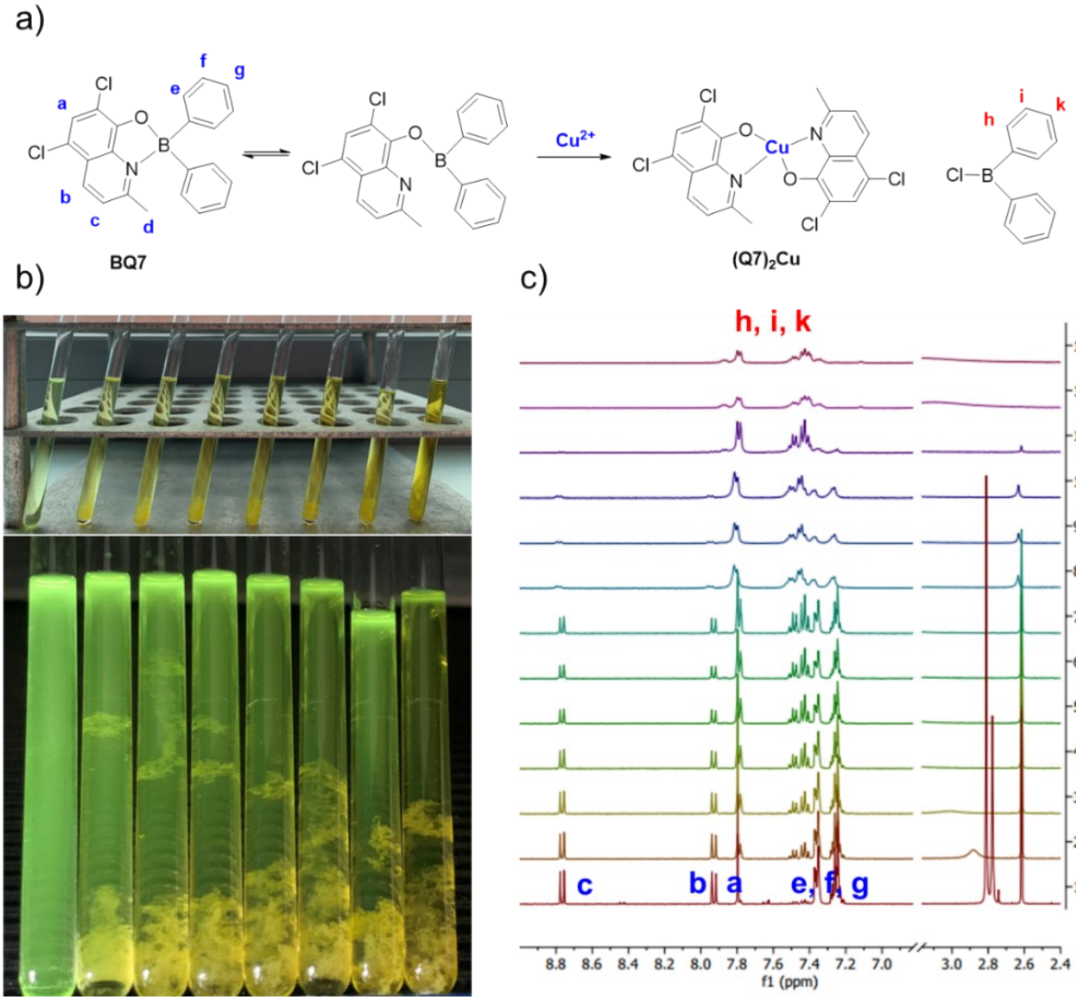

Figure S11. a) Proposal Cu^{2+} sensing mechanism of **BQ7**; b) Image of **BQ7** (2.5 mM) in acetone-d_6 in the presence of Cu^{2+} (0 – 1.0 eq) under white light and 365 nm light; c) ^{1}H-NMR spectra of **BQ7** (2.5 mM) in acetone-d_6 in the presence of Cu^{2+} (0 – 1.0 eq).

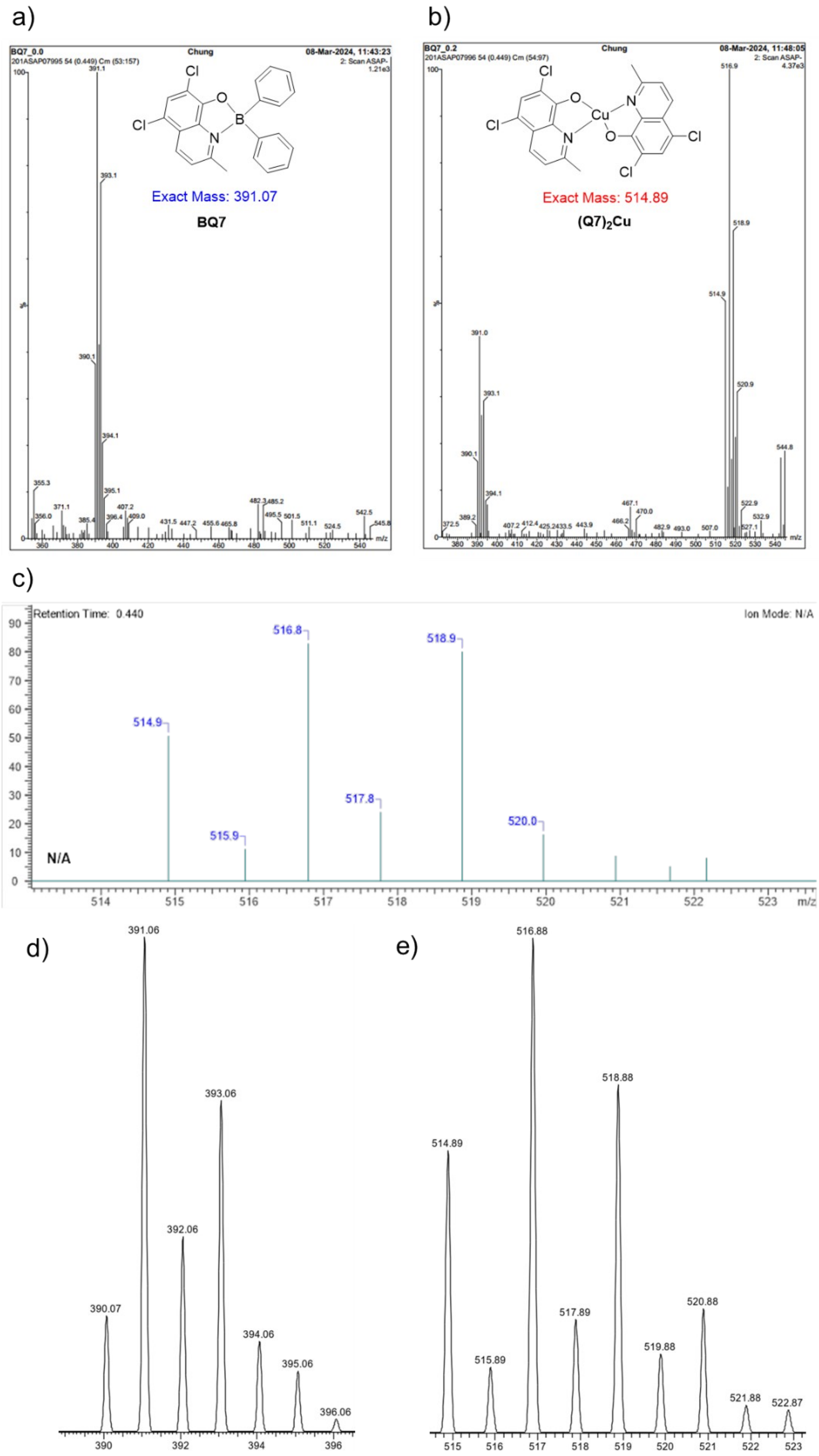

Figure S12. MS spectra of **BQ7** before (a) and after (b, c) adding Cu^{2+} (0.2 eq); simulated isotopic patterns for fragments (d) $[\mathbf{BQ7}]^-$ and (e) $[\mathbf{Cu(Q7)_2}]^-$.

5. Computational investigations.

The geometries of the ground states (S_0) of **BQ1-BQ7** were optimized with Density Functional Theory (DFT).[1] To model the UV-Vis absorption and emission spectra, the 6-31+G(d,p) basis set[2] was employed in combination with the LanL2DZ basis set[3] specifically for the iodine atom.18 functionals were tested and MPW1PW91 functional demonstrates the highest concordance of computed excitation with experimental UV-Vis absorption wavelength (see **Table S4**). Subsequently, the geometry of singlet and triplet excited states were optimized using Time-dependent DFT (TD-DFT) in combination with the Tamm-Dancoff Approximation (TDA).[4] All these calculations were conducted using the Gaussian 16 package. [5]

Spin-orbit couplings (SOC) between the first singlet (S_1) and triplet (T_1) excited states were computed at the T_1 optimized geometry. For these SOC calculations, the Spin-Orbit Mean-Field (SOMF) method,[6] in conjunction with the Resolution of Identity (RI),[7] was employed to expedite the computation of Coulomb integrals. Furthermore, the intersystem crossing (ISC) rate constant from S_1 to T_1 was calculated using the Adiabatic Hessian (AH) model,[8] incorporating the Franck-Condon (FC) and Herzberg-Teller (HT) effects.[9] To enhance the accuracy of the SOC and ISC calculations,[10] the CAM-B3LYP functional[11] was applied due to accurate description of charge-transfer excitations[12] and balanced accuracy for valence and Rydberg state.[13] Salar relativistic effects were included through the Zero-Order Relativistic Approximation (ZORA).[14] The RIJCOSX approximation was applied,[15] with the ZORA-def2-TZVP basis sets and SARC-ZORA-TZVP basis set for the iodine atom. ISC and SOC calculations were performed with the ORCA software.[16] In addition, fluorescence rate constants were determined using FCclasses3,[17] which also utilized the AH model,[8] in the contribution of FC-HT effect.[9] These calculations were performed in Cartesian coordinates under the TD approximation, and a Lorentzian half-width at half-maximum (HWHM) broadening of 0.01 eV was applied. Finally, solvent effects of all above calculation were modelled with the Polarizable Continuum Model (PCM).[18]

We performed quantum mechanics/molecular mechanics (QM/MM) simulations utilizing a multilayer ONIOM[19] within the Gaussian 16 computational package.[5] In its crystalline form, **BQ7** exhibits a π-π stacking interactions between the quinoline and phenyl moieties of two adjacent molecules. Accordingly, these two interacting molecules (**BQ7** dimer) were designated as the high-layer QM region, while the surrounding molecular environment was treated as the low-layer MM region. The initial molecular coordination structure for QM/MM optimizations was extracted from single-crystal X-ray diffraction (SC-XRD) data. To approximately model the stacking arrangement in the aggregated state, the **BQ7** dimer in the QM layer was allowed to undergo unrestricted fluctuations within the MM layer, whereas the motion of the remaining **BQ7** molecules was constrained during the simulation. The ground-state (S_0) and excited-state (S_1 and T_1) geometries of the **BQ7** dimer were optimized using DFT and TDA TD-DFT, employing the MPW1PW91 functional with the 6-31+G(d,p) basis set in PCM for water as the solvent. The MM layer was parameterized using the universal force field (UFF) in conjunction with the charge equilibration (Qeq) method.[20] Additionally, spin-orbit coupling (SOC) between the S_1 and T_1 states of the **BQ7** dimer was computed using the same theoretical protocol as applied to the monomer.

Table S3. Excitation wavelength (nm) of **BQ1**-**BQ7** was computed by TDA TD-DFT using (1) APFD, (2) B3LYP, (3) B3PW91, (4) BhandHLYP, (5) BVP86, (6) CAM-B3LYP, (7) HCTH, (8) HSEH1PBE, (9) LC-ωPBE, (10) LSDA, (11) M06, (12) M062X, (13) M06HF, (14) M06L, (15) MPW1PW91, (16) PBE, (17) TPSSTPSS, (18) wB97XD at 6-31+G(d,p) basic set with PCM for toluene. Mean absolute deviation (MAD). LanL2DZ basis set is applied for the iodine atom.

	BQ1	**BQ2**	**BQ3**	**BQ4**	**BQ5**	**BQ6**	**BQ7**	**MAD**
1	414	434	437	439	440	441	430	21
2	429	448	449	453	455	454	442	35
3	426	446	449	452	453	453	442	34
4	346	357	355	356	357	357	347	58
5	508	539	547	553	557	555	543	131
6	364	377	375	376	376	377	367	39
7	500	531	539	545	549	547	534	123
8	416	437	440	443	444	444	432	24
9	325	335	333	333	330	332	324	82
10	498	534	545	551	560	555	539	128
11	415	370	371	373	439	374	364	35
12	357	308	306	308	376	307	299	89
13	300	488	495	497	309	502	489	88
14	460	435	435	431	502	437	430	35
15	**410**	**429**	**431**	**433**	**434**	**434**	**423**	**16**
16	509	541	550	555	560	558	544	133
17	490	517	523	528	531	530	518	108
18	363	376	374	374	372	374	366	41
Exp.	400	414	412	415	421	419	405	

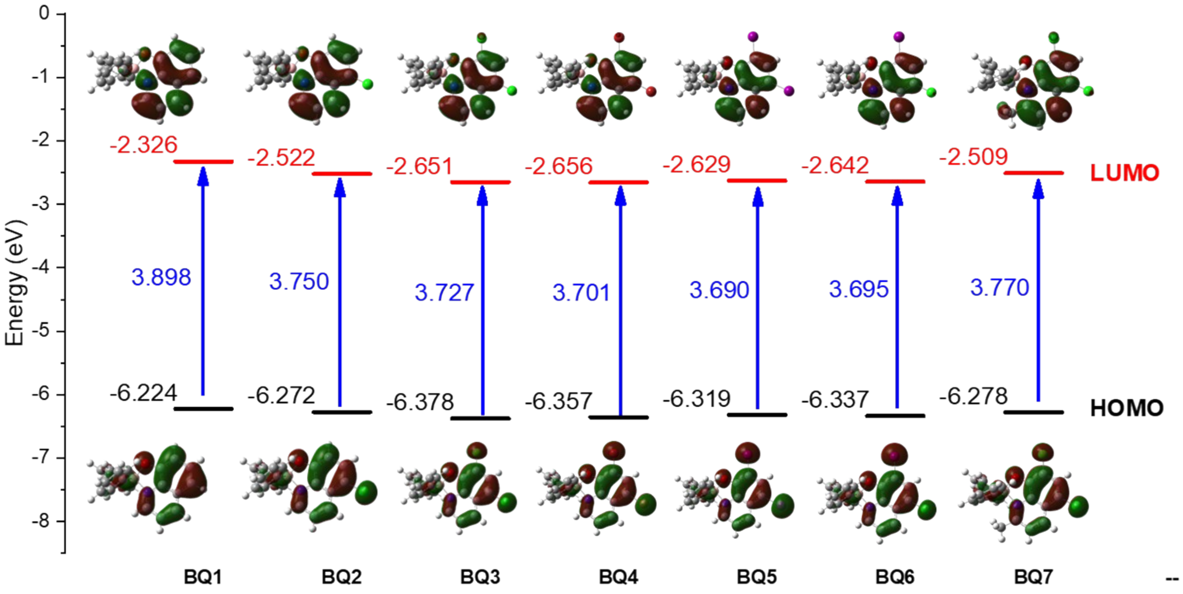

Figure S13. HOMO and LUMO image and energy along with its energy gap (ev) of **BQ1-BQ7** at S_0 geometry, which was optimized by DFT method using MPW1PW91 functional and 6-31+g(d,p) in PCM for toluene solvent (LanL2DZ basis set is applied for the iodine atom).

Table S4. Computed S_1 absorption and S_1 emission properties of **BQ1** – **BQ7** at S_0 and S_1 geometry, respectively, which was optimized by TD and TDA TD-DFT, respectively using MPW1PW91/6-31+g(d,p) level of theory in PCM for toluene. **BQ7***: **BQ7** dimer state in QM/MM calculations, their S_0 and S_1 geometry were optimized by DFT and TDA TD-DFT method, respectively using MPW1PW91/6-31+g(d,p) level of theory in PCM for water (see more detail in computational method). Vertical energy (E_{vt}); absorption wavelength (λ_{abs}); emission wavelength (λ_{ems}); oscillator strength (f).

	$S_0 \rightarrow S_1$ transition				$S_1 \rightarrow S_0$ transition			
	E_{vt} (ev)	λ_{abs} (nm)	f	Transition	E_{vt} (ev)	λ_{ems} (nm)	f	Transition
BQ1	3.02	410	0.09	H → L (98.5 %)	2.38	520	0.07	H → L (99.0 %)
BQ2	2.89	429	0.10	H → L (98.7 %)	2.23	556	0.07	H → L (99.2 %)
BQ3	2.88	431	0.10	H → L (98.6 %)	2.23	556	0.07	H → L (99.1 %)
BQ4	2.86	433	0.10	H → L (98.6 %)	2.24	554	0.07	H → L (99.2 %)
BQ5	2.85	434	0.09	H → L (98.7 %)	2.26	549	0.07	H → L (99.2 %)
BQ6	2.85	434	0.09	H → L (98.6 %)	2.23	556	0.07	H → L (99.1 %)
BQ7	2.93	423	0.09	H → L (98.6 %)	2.25	551	0.07	H → L (99.2 %)
BQ7*					2.46	504	0.12	H → L (96.6 %)

Table S5. Excited state properties of **BQ1** – **BQ7** at T_1 and T_2 geometry, which were optimized by TDA TD-DFT method using MPW1PW91/6-31+g(d,p) level of theory in PCM for toluene. **BQ7***: **BQ7** dimer state in QM/MM calculations, their T_1 and T_2 geometry were optimized by TDA TD-DFT, respectively using MPW1PW91/6-31+g(d,p) level of theory in PCM for water (see more detail in computational method). Vertical energy (E_{vt}); emission wavelength (λ_{ems}).

	T_1			T_2		
	E_{vt} (ev)	λ_{ems} (nm)	Transition	E_{vt} (ev)	λ_{ems} (nm)	Transition
BQ1	1.28	970	H → L (98.5 %)	3.09	402	H-1 → L (93.3 %)
BQ2	1.18	1050	H → L (99.5 %)	2.95	420	H-1 → L (95.1 %)
BQ3	1.20	1031	H → L (98.5 %)	2.91	427	H-1 → L (94.3 %) H → L (2.5 %)
BQ4	1.24	1003	H → L (97.6 %)	2.13	581	H→ L (79.1 %) H-1 → L (19.1 %)
BQ5	1.28	966	H → L (96.0 %)	2.14	581	H→ L (79.8 %) H-1 → L (18.5 %)
BQ6	1.22	1017	H → L (97.5 %) H → L+3 (2.1 %)	2.13	582	H-1→ L (79.7 %) H → L (19.5 %)
BQ7	1.22	1019	H → L (98.1 %)	2.93	423	H-1→ L (94.7 %)
BQ7*	1.66	749	H → L (95.1 %)			

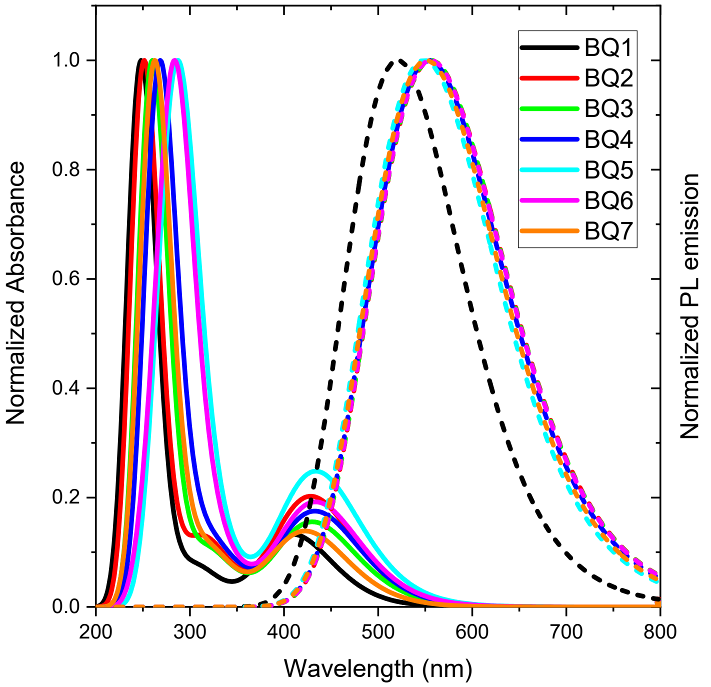

Figure S14. Computed absorbance and emission intensity of **BQ1** – **BQ7** at S_0 and S_1 geometry, respectively, which was optimized by TD and TDA TD-DFT, respectively using MPW1PW91/6-31+g(d,p) level of theory in PCM for toluene.

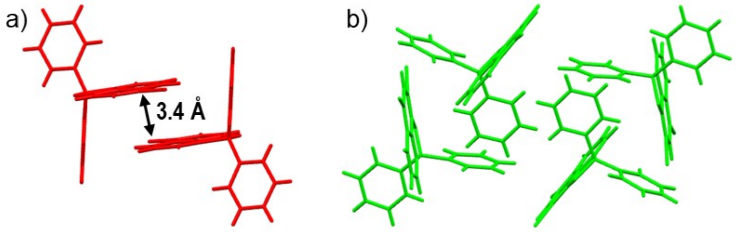

Figure S15. Partial crystal packing of a) **BQ2**, b) **BQ6** and c) **BQ7**.

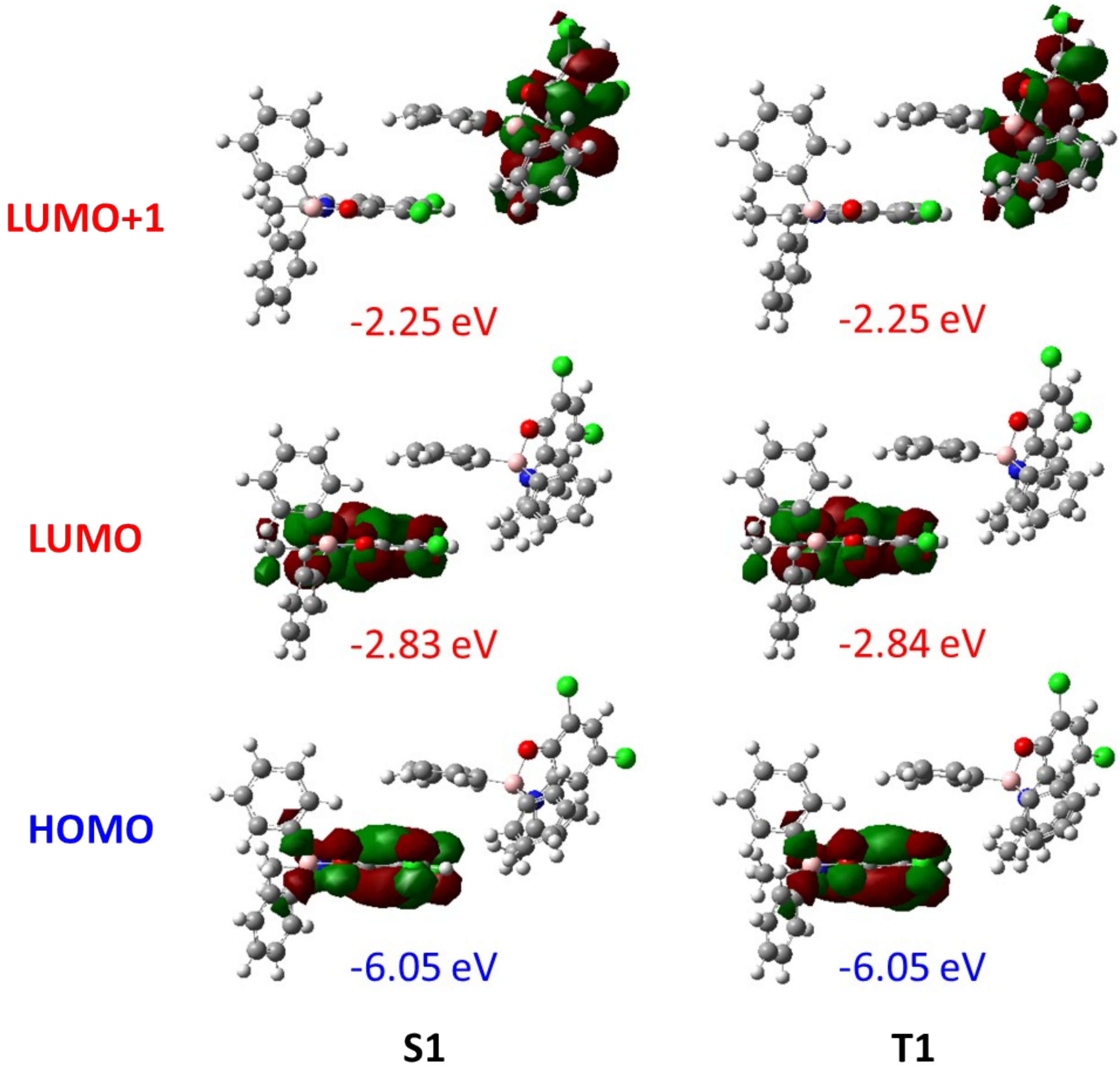

Figure S16. MO image and energy level of **BQ7** dimer at S_0, S_1, and T_1 geometry, which were optimized by TD and TDA TD-DFT, respectively using MPW1PW91/6-31+g(d,p) level of theory in PCM for water (see more detail in computational method).

6. *In vitro* experiments.

Cell culture

A human cervical adenocarcinoma cell line, HeLa, was obtained from Korean Cell Line Bank and were grown in Dulbecco's Modified Eagle Medium (DMEM, Welgene) supplemented with fetal bovine serum (FBS, Welgene), 4 mM L-glutamine, 100 U/mL penicillin, 100 µg/mL streptomycin and 0.25 µg/mL amphotericin B (Welgene) maintained at 37°C and 5% CO_2. Cells were seeded on confocal dish (SPL, #104350) overnight before the experiments.

Fluorescence staining and confocal laser scanning microscope (CLSM) imaging

The HeLa cells were incubated with 100 µM BQ7, 50 µM LysoTracker Deep Red, 100 µM MitoTracker Deep Red, 100 nM MitoTracker Green, 2 µM/mL Hoechst 33342, 1 µM BODIPY 493/503 or 5 µM BODIPY 581/591 C11 (Invitrogen). The confocal images were obtained using LSM 780, Axio observer.Z1 / 7 microscope with Plan-Apochromat 63x/1.40 Oil M27 objective lens (Zeiss). 405 nm wavelength laser was used for **BQ7** and Hoechst 33342 detection, 488 nm for MitoTracker Green and BODIPY 493/503, and 640 nm for LysoTracker Deep Red and MitoTracker Deep Red. For BODIPY 581/591 detection, 488 nm and 561 nm laser was used. When applicable, T-PMT channel was obtained for brightfield images. The images were analyzed using ImageJ, and the Pearson colocalization coefficient was calculated using EzColocalization plugin.[21]

Copper sensing of BQ7

The HeLa cells stained with **BQ7** were imaged in DMEM cell culture medium, and then $CuCl_2$ was added to the medium to the final concentration of 100 µM. The images were taken with the same setting at 400 s after the $CuCl_2$ treatment.

ROS and superoxide anion generation

The **BQ7**-stained HeLa cells were irradiated with 400 nm light using LED panel. 20 µM DCFH-DA (Sigma-Aldrich) and 10 µM DHE (Invitrogen) were stained for 30 minutes to probe for ROS and superoxide anion, respectively. For delayed ROS detection, DCFH-DA was stained 270 minutes after the light irradiation.

Photo(cytotoxicity) of BQ7 and $(Q7)_2Cu$

HeLa cells were seeded at 20,000 cells/cm^2 in 96-well cell culture plate. 0, 10, 30 and 100 µM **BQ7** was treated to the cells. The 400 nm light was irradiated for 30 minutes for photodynamic experiment, and the 0, 30 and 100 µM $CuCl_2$ was treated for chemotherapy experiment. After changing to fresh cell culture medium, the cells were incubated at 37°C with 5% CO_2. For hypoxia condition experiment, all possible incubation processes were done in 1% O2, using the modular incubator chamber (Embrient Inc). After 24 hours of incubation, the cells were incubated with CCK-8 solution (Dojindo Laboratories) for 1 hour and optical density was measured using Synergy HTX Multimode Microplate Reader (BioTek) at 450 nm.

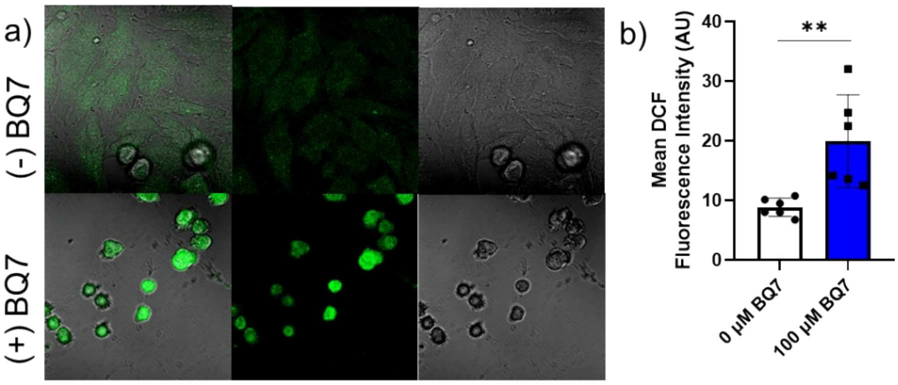

Figure S17. Fluorescence image (a) and intensity (b) of DCF in the absence and presence of **BQ7** under light irradiation.

Structural spectra

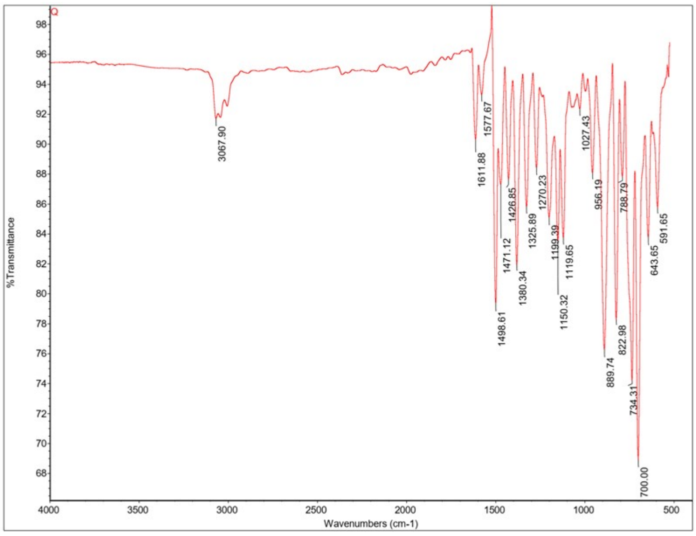

Figure S18. IR spectrum of **BQ1**.

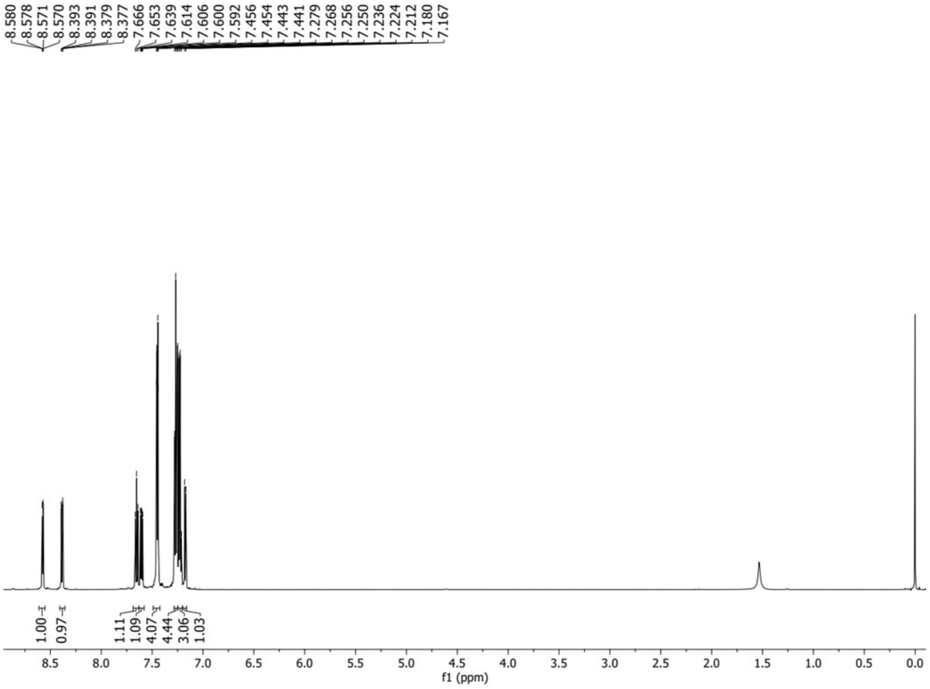

Figure S19. ^{1}H NMR spectrum of **BQ1**.

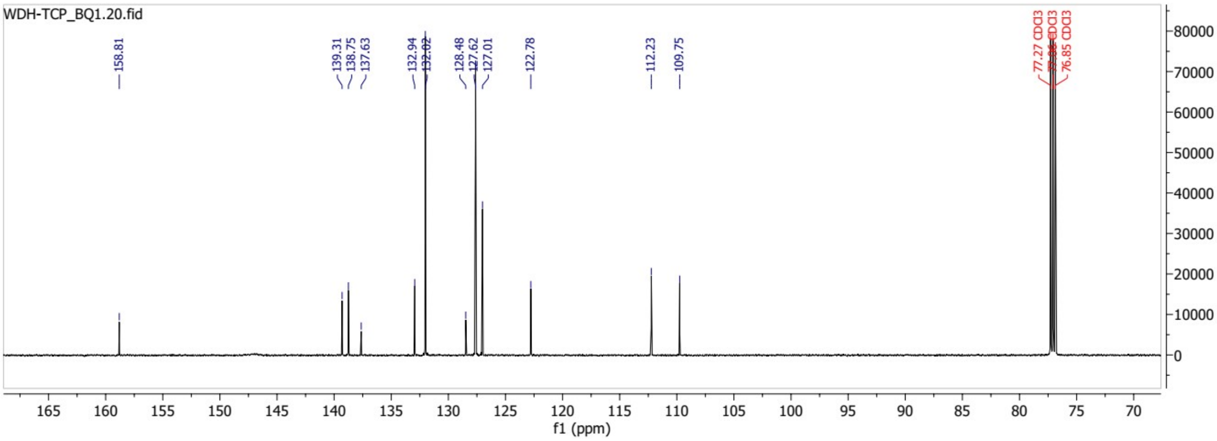

Figure S20. ^{13}C NMR spectrum of **BQ1**.

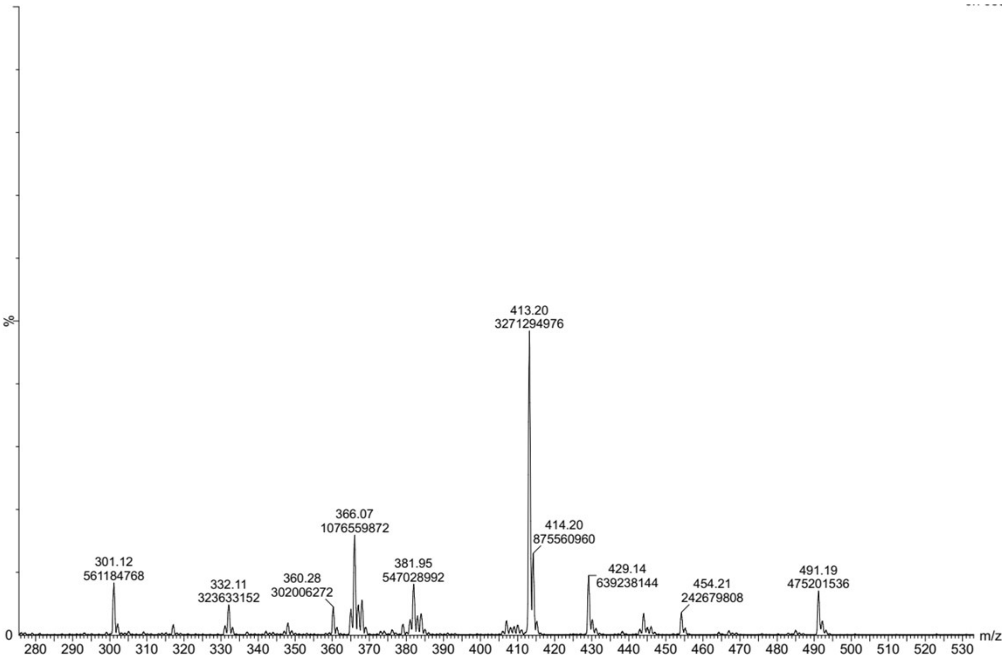

Figure S21. Part of the positive mode ESI mass spectrum of **BQ2**.

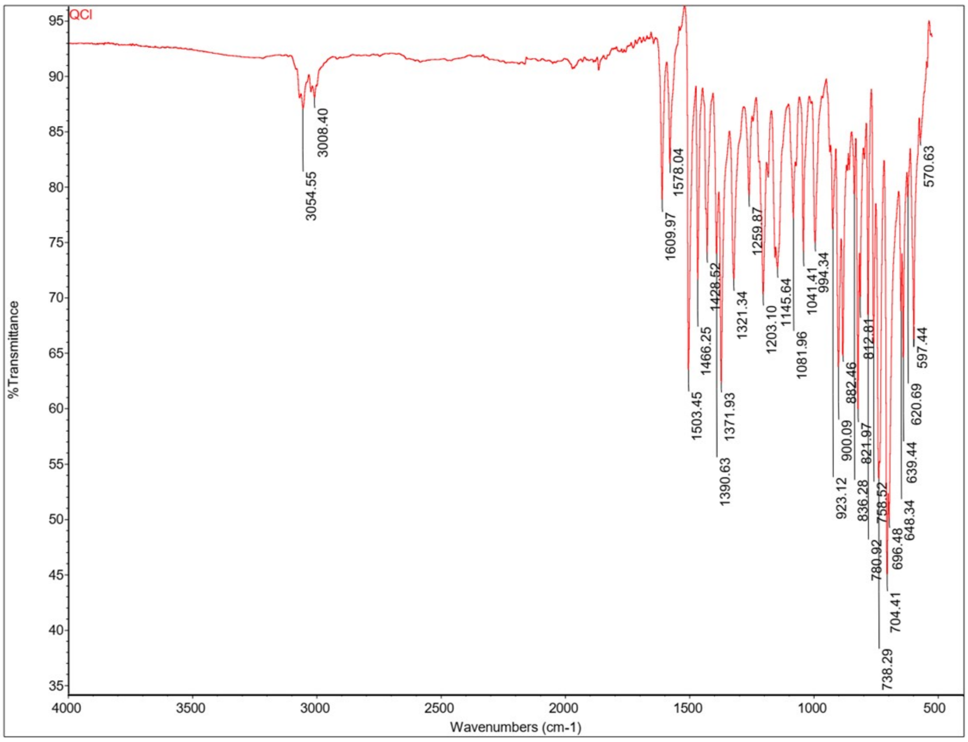

Figure S22. IR spectrum of **BQ2**.

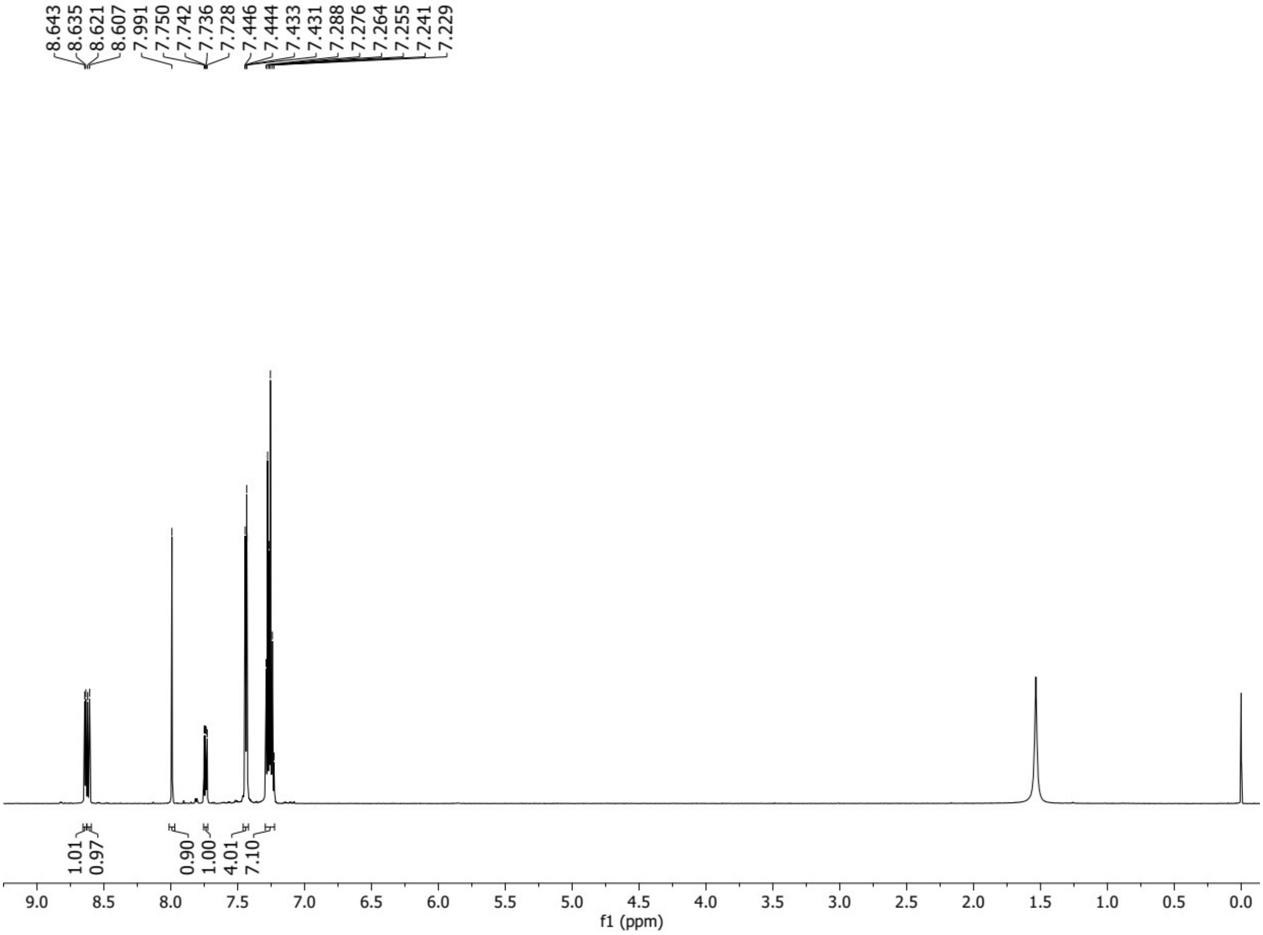

Figure S23. ^{1}H NMR spectrum of **BQ2**.

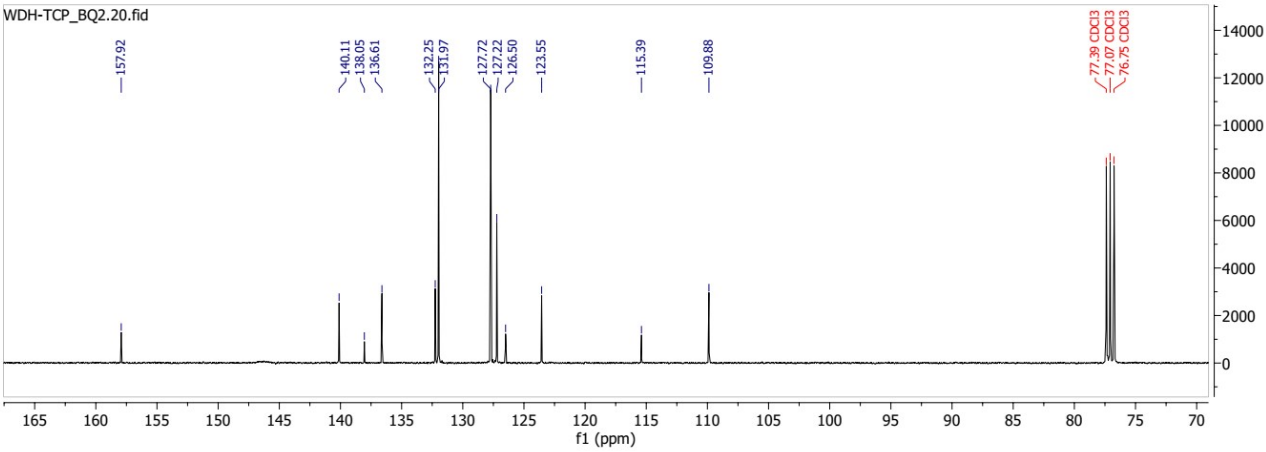

Figure S24. ^{13}C NMR spectrum of **BQ2**.

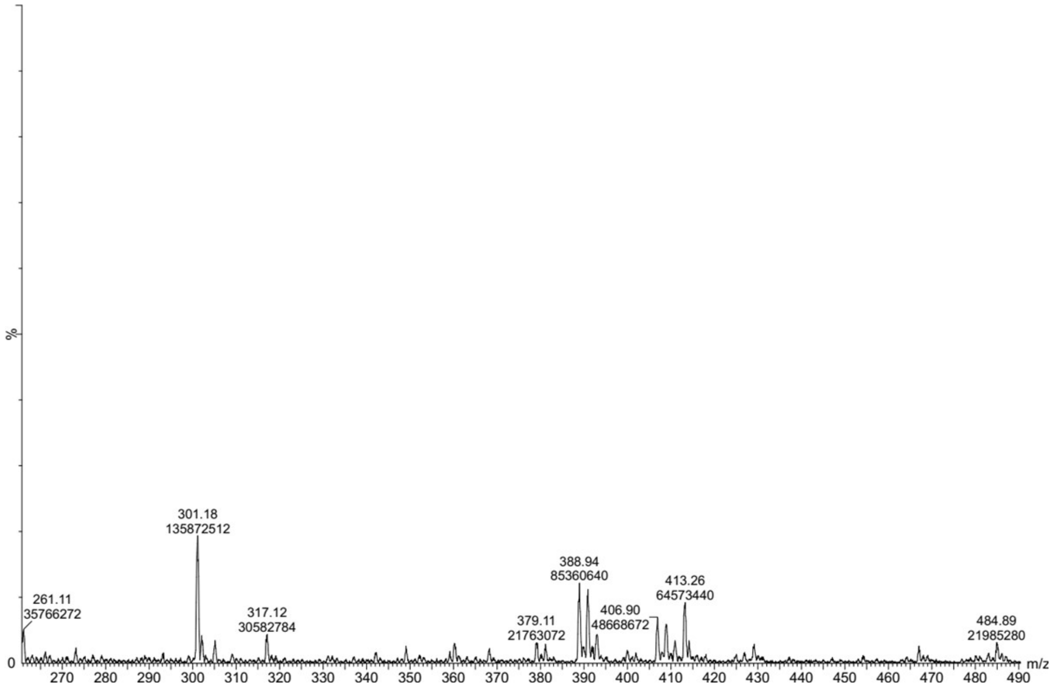

Figure S25. Part of the positive mode ESI mass spectrum of **BQ3**.

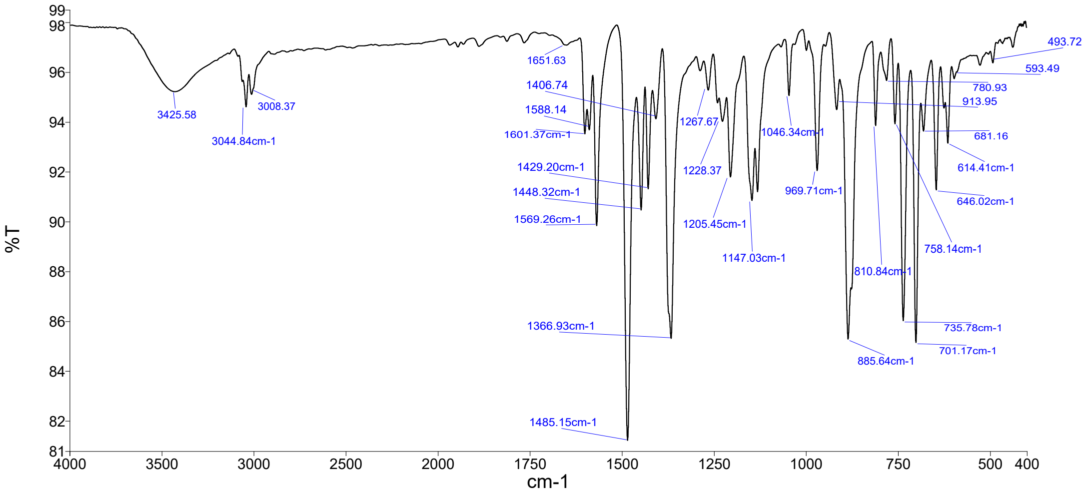

Figure S26. IR spectrum of **BQ3**.

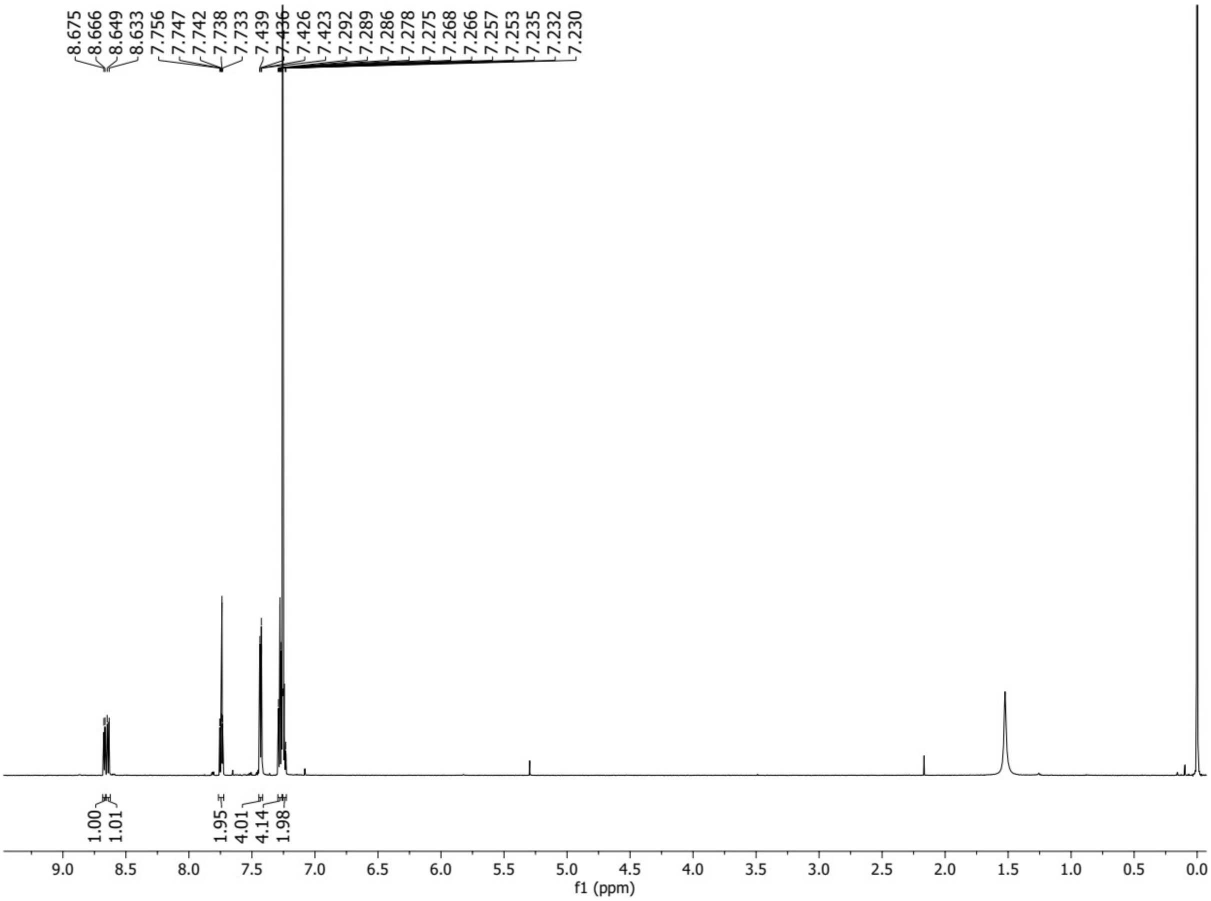

Figure S27. ^{1}H NM spectrum of **BQ3**.

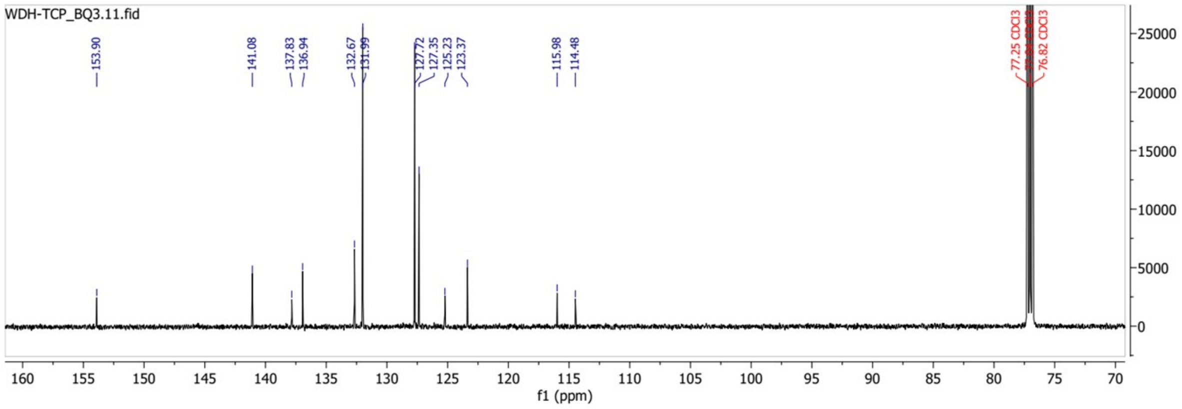

Figure S28. ^{13}C NM spectrum of **BQ3**.

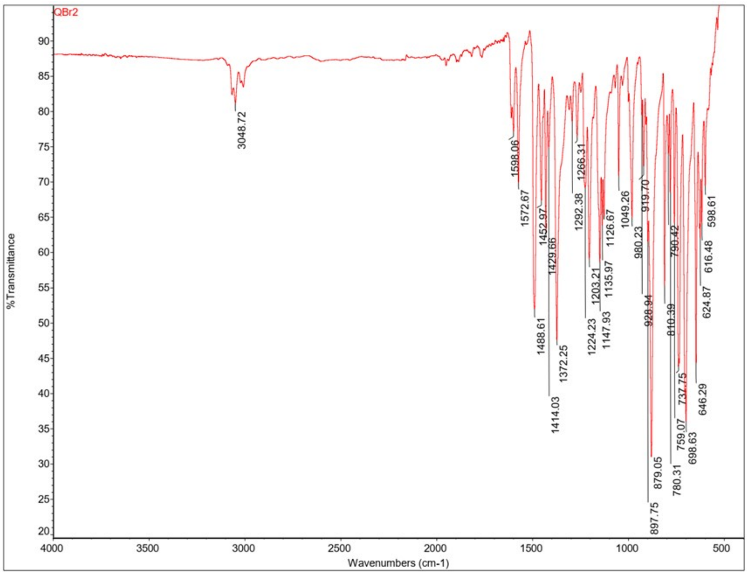

Figure S29. IR spectrum of **BQ4**.

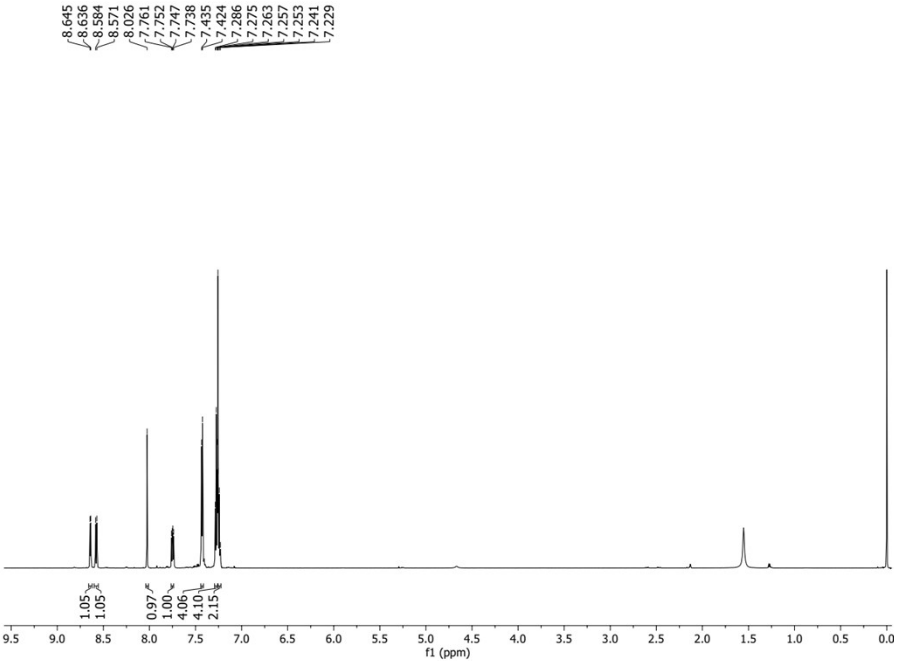

Figure S30. ^{1}H NMR spectrum of **BQ4**.

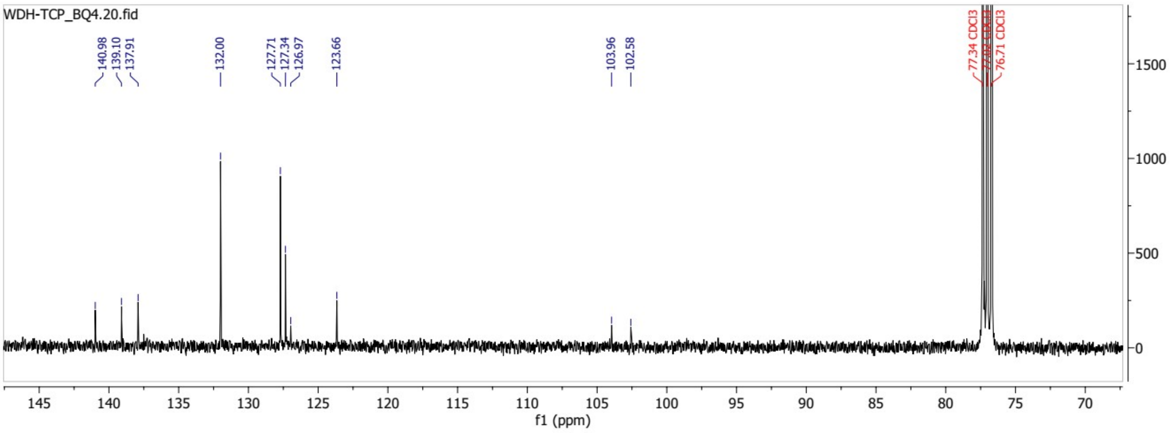

Figure S31. ^{13}C NMR spectrum of **BQ4**.

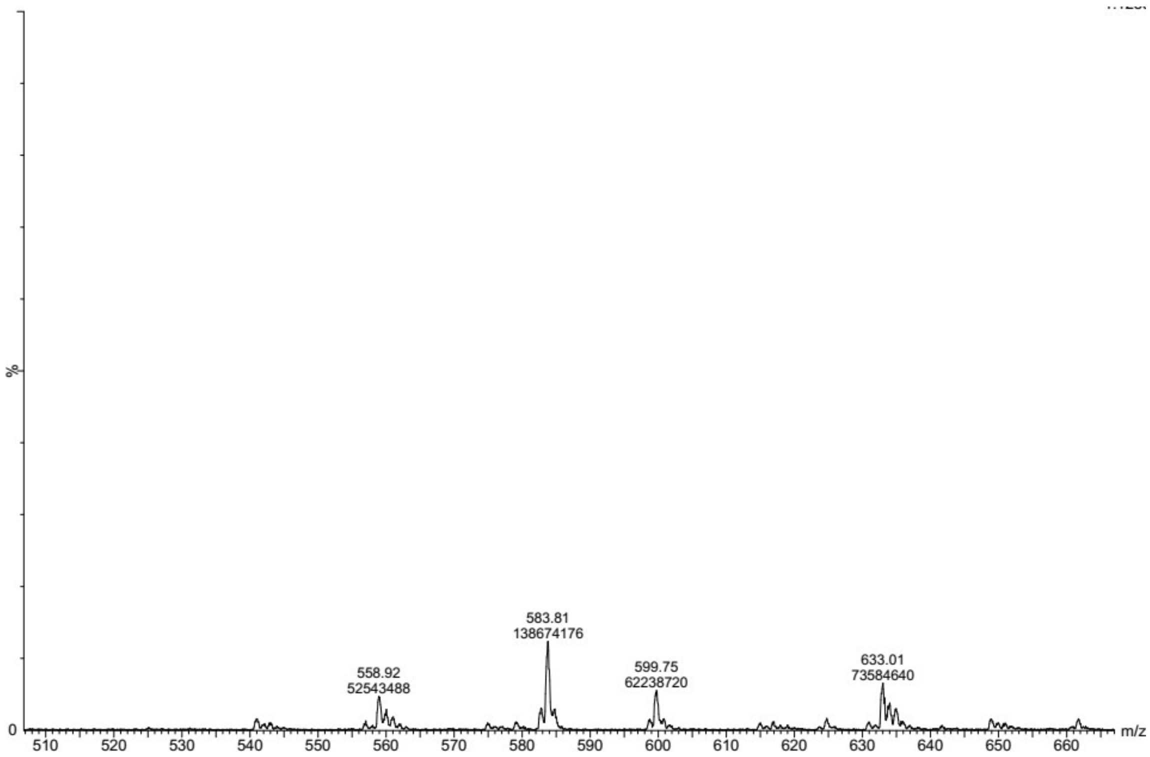

Figure S32. Part of the positive mode ESI mass spectrum of **BQ5**.

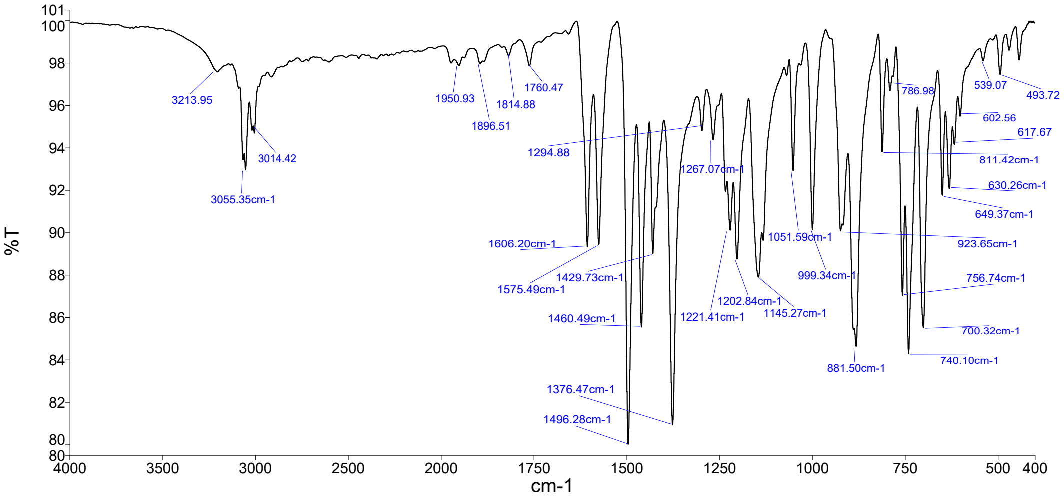

Figure S33. IR spectrum of **BQ5**.

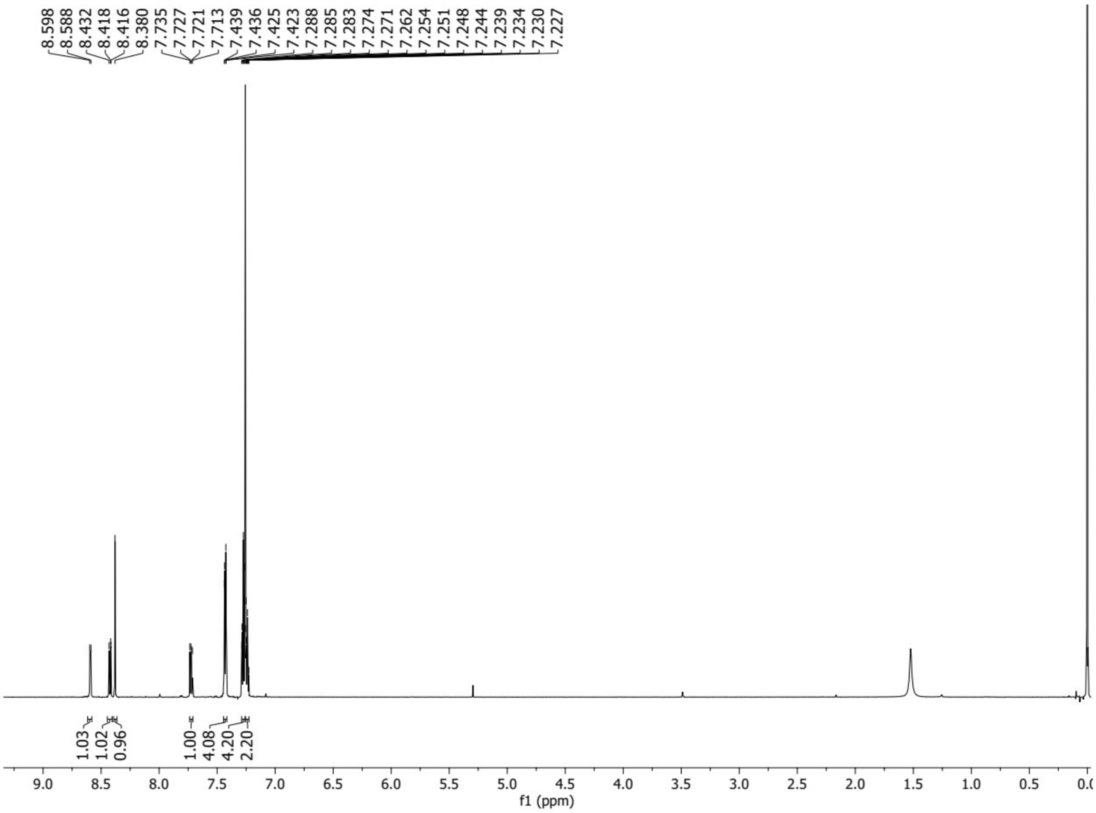

Figure S34. ^{1}H NMR spectrum of **BQ5**.

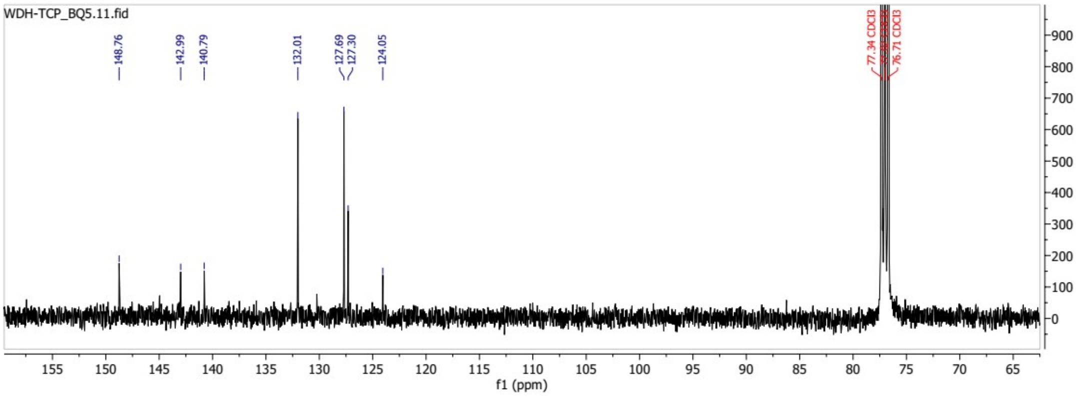

Figure S35. ^{1}H NMR spectrum of **BQ5**.

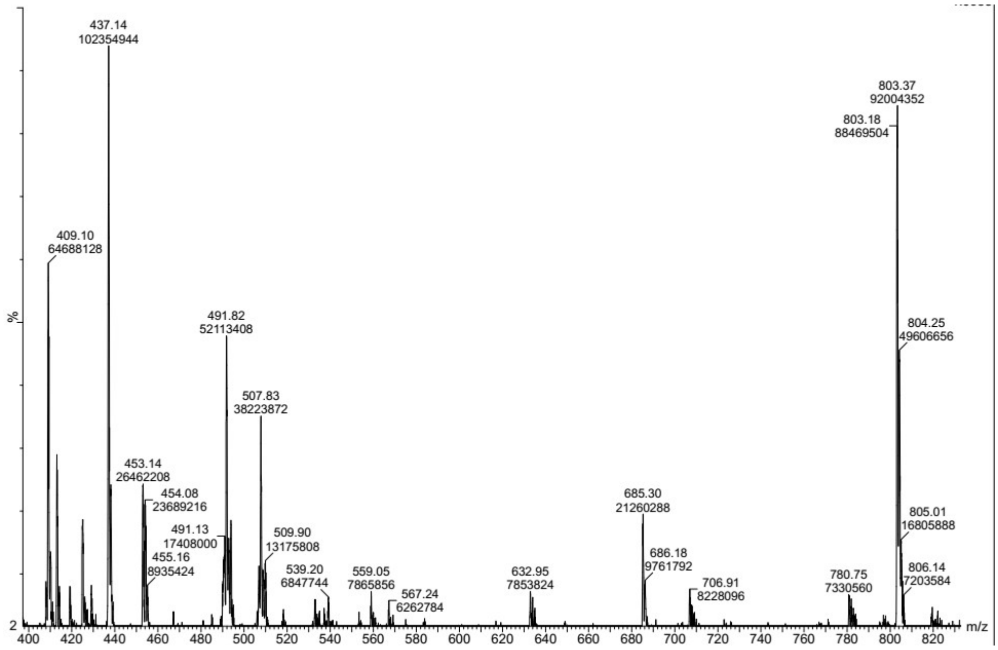

Figure S36. Part of the positive mode ESI mass spectrum of **BQ6**.

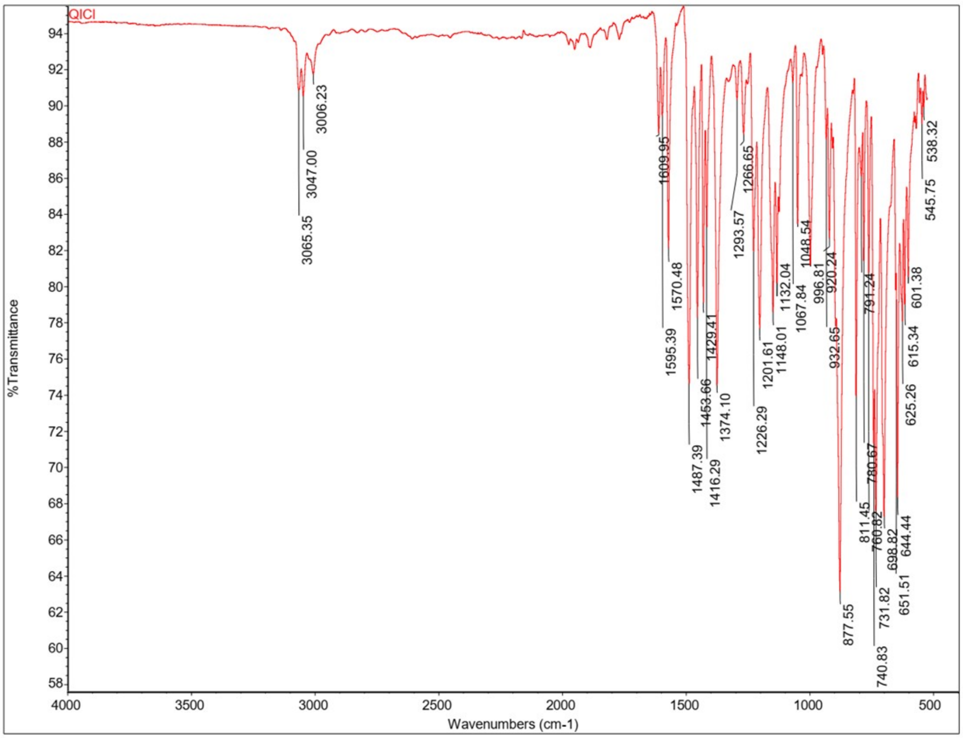

Figure S37. IR spectrum of **BQ6**.

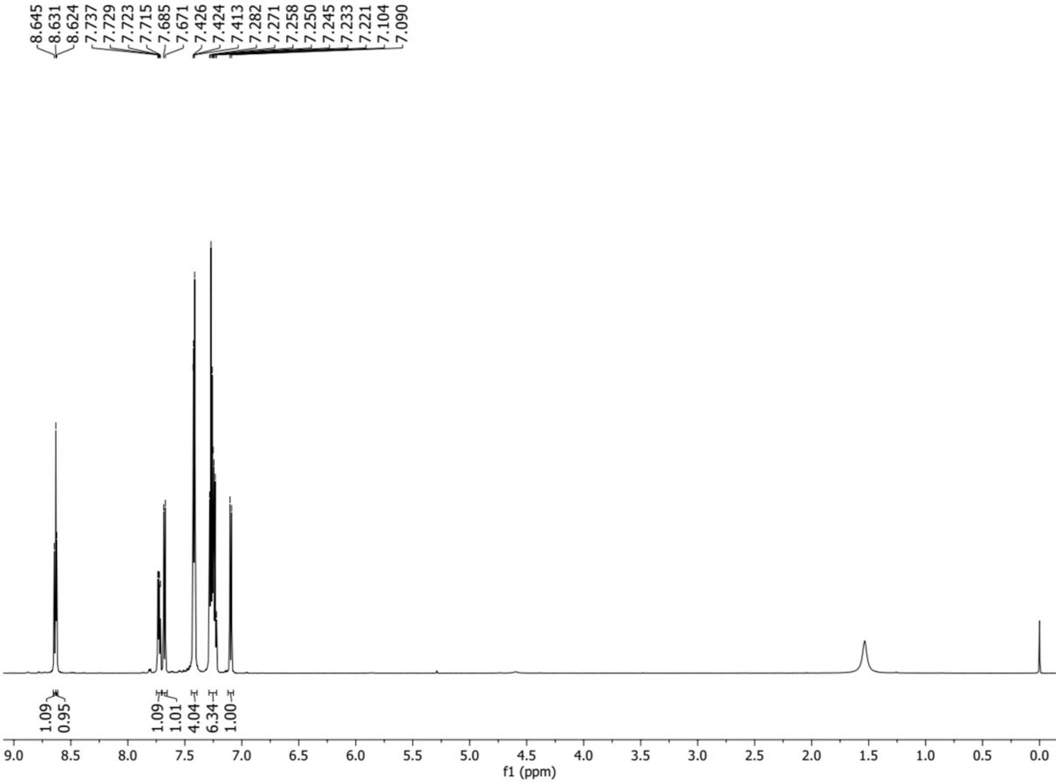

Figure S38. ^{1}H NMR spectrum of **BQ6**.

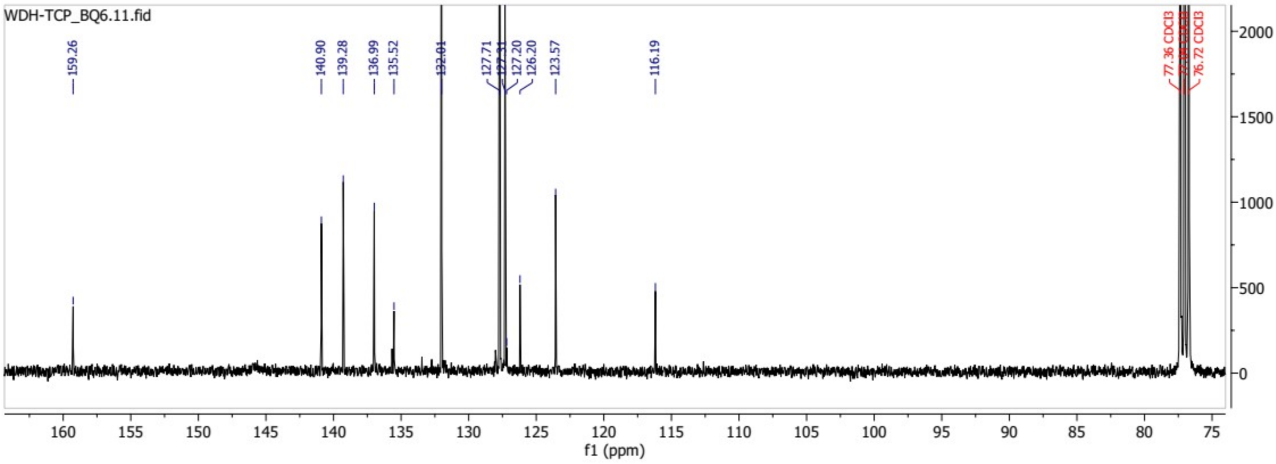

Figure S39. ^{13}C NMR spectrum of **BQ6**.

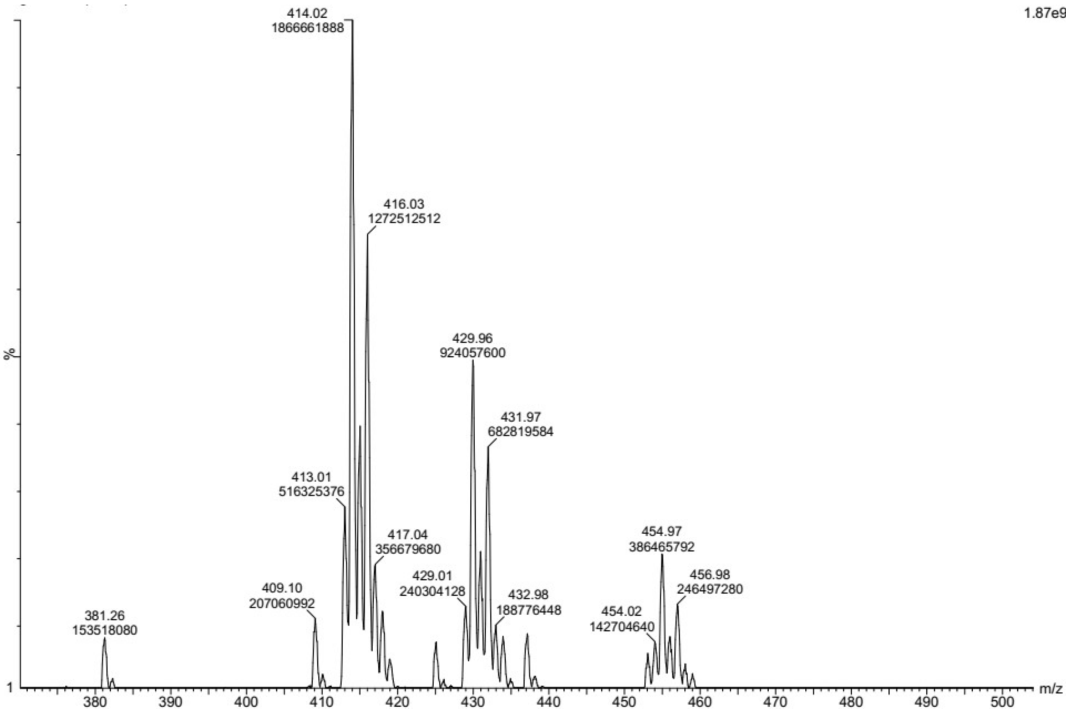

Figure S40. Part of the positive mode ESI mass spectrum of **BQ7**.

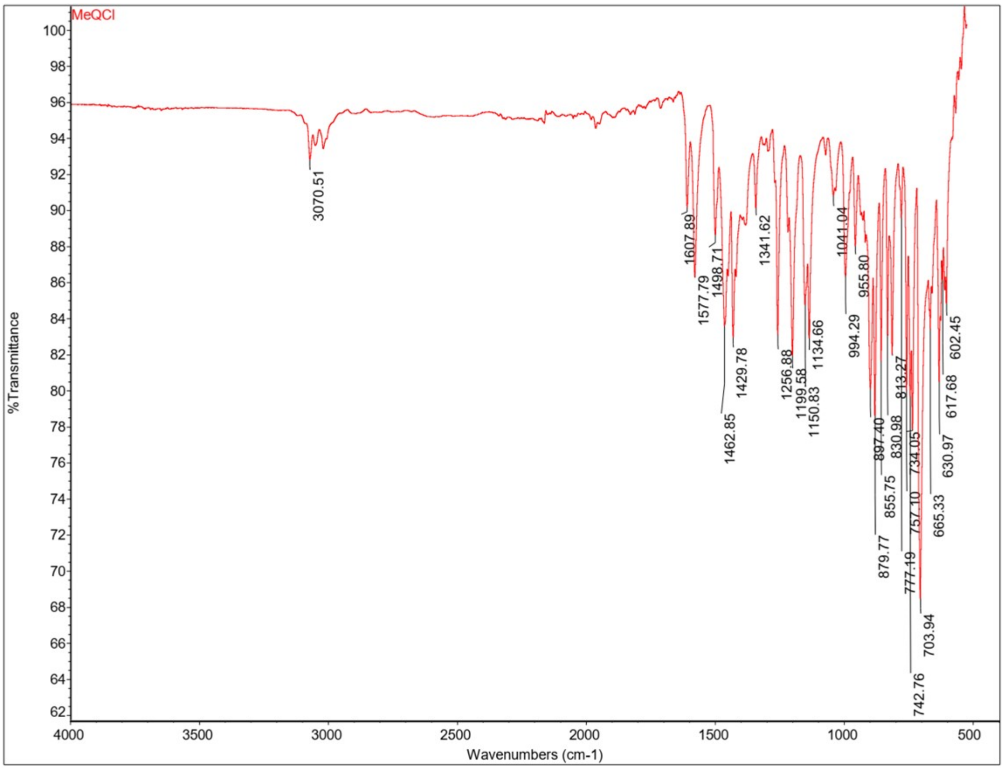

Figure S41. IR spectrum of **BQ7**.

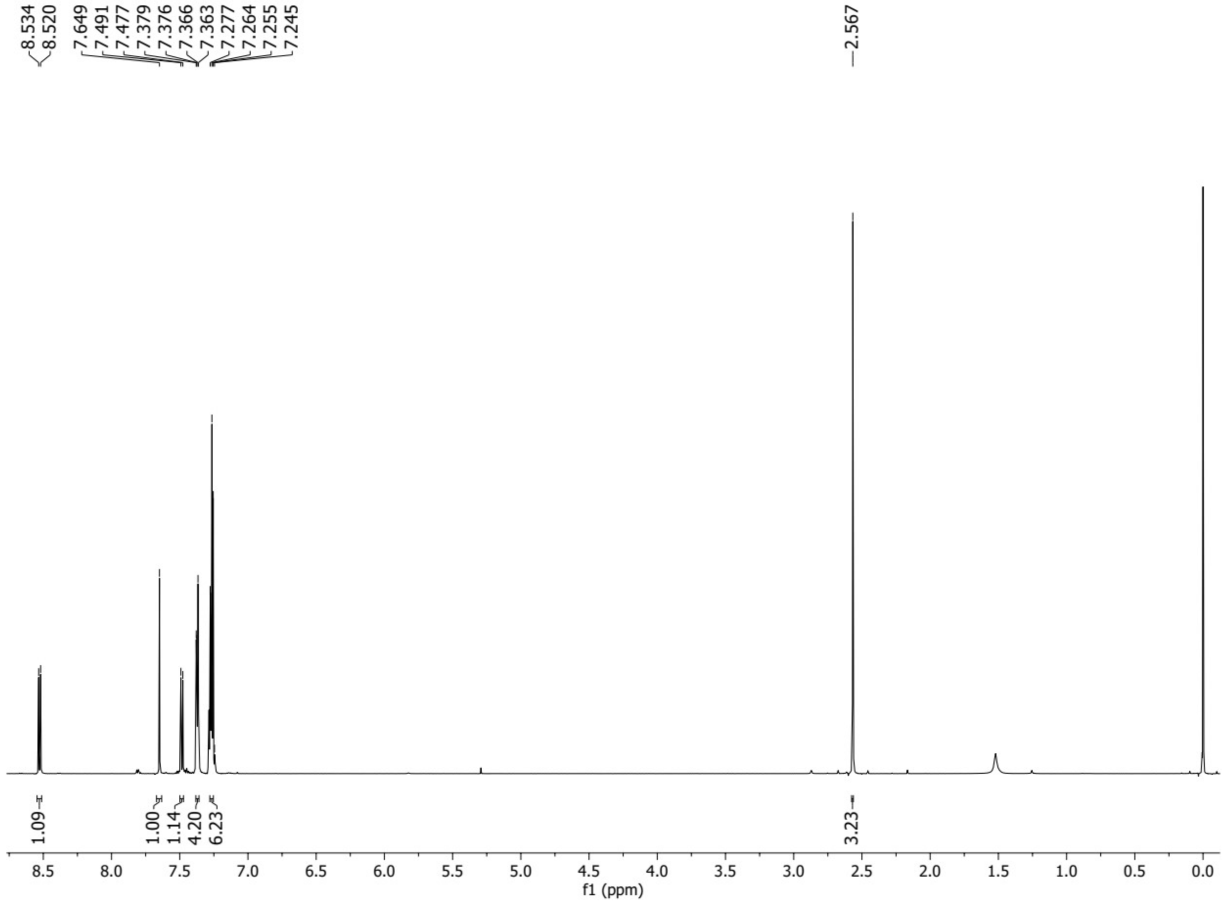

Figure S42. ^{1}H NMR spectrum of **BQ7**.

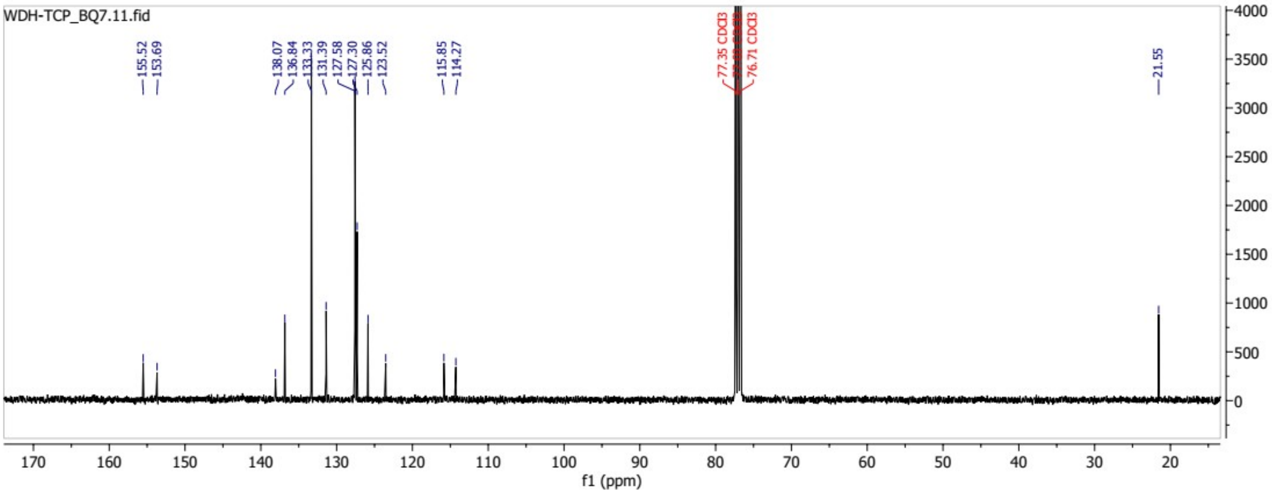

Figure S43. ^{13}C NMR spectrum of **BQ7**.

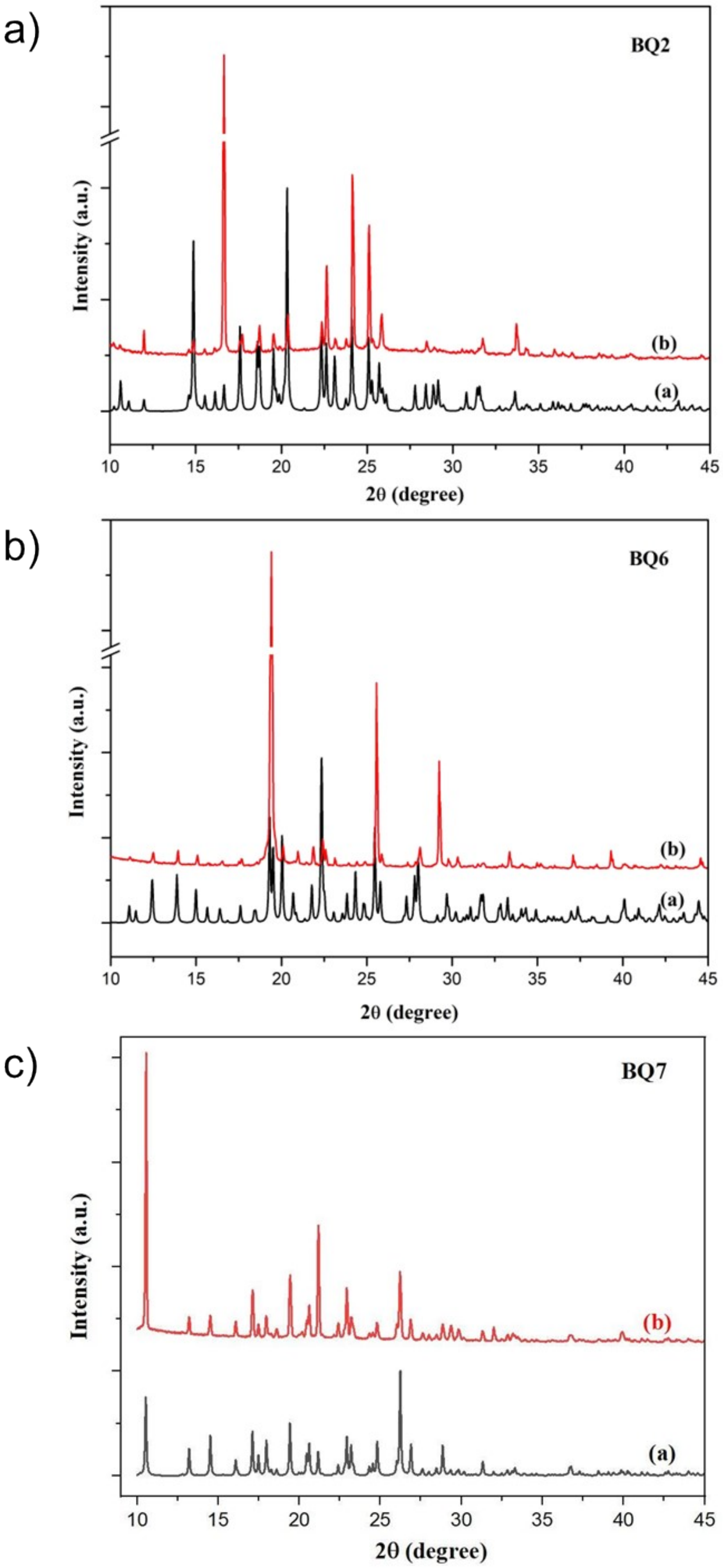

Figure S44. Powder XRD from (a) SC-XRD and (b) powder XRD of **BQ2**, **BQ6** and **BQ7**. The powder XRD sample of **BQ7** was obtained from crushed crystal fragments after SC-XRD measurement. While the power XRD samples of **BQ2** and **BQ6** were obtained from available solid samples.

Table S6. Crystal data and structure refinement for **BQ2**, **BQ6** and **BQ7**.

Complex	**BQ2**	**BQ6**	**BQ7**
Empirical formula	$C_{21}H_{15}BClNO$	$C_{21}H_{14}BClINO$	$C_{22}H_{16}BCl_2NO$
Formula weight	343.60	469.49	392.07
Temperature/K	293(2)	293(2)	273(2)
Crystal system	monoclinic	monoclinic	orthorhombic
Space group	$P2_1/c$	$P2_1/n$	Pbca
a/Å	11.6261(9)	9.0115(3)	16.7740(9)
b/Å	14.7545(10)	18.3724(8)	12.1914(7)
c/Å	11.0120(9)	11.5145(5)	18.2466(10)
α/°	90	90	90
β/°	113.782(9)	100.784(4)	90
γ/°	90	90	90
Volume/$Å^3$	1728.6(3)	1872.71(13)	3731.4(4)
Z	4	4	8
$\rho_{calc}g/cm^3$	1.320	1.665	1.396
μ/mm^{-1}	0.229	1.862	0.360
F(000)	712.0	920.0	1616.0
Crystal size/mm^3	0.5 × 0.5 × 0.25	0.35 × 0.35 × 0.2	0.49 × 0.17 × 0.09
Radiation	Mo Kα (λ = 0.71073 Å)	Mo Kα (λ = 0.71073 Å)	Mo Kα (λ = 0.71073 Å)
2Θ range for data collection/°	4.896 to 52.744	5.108 to 52.744	5.082 to 52.736
Index ranges	$-14 \leq h \leq 14$, $-18 \leq k \leq 18$, $-13 \leq l \leq 13$	$-11 \leq h \leq 11$, $-19 \leq k \leq 22$, $-13 \leq l \leq 14$	$-20 \leq h \leq 20$, $-14 \leq k \leq 15$, $-22 \leq l \leq 22$
Reflections collected	17521	11714	59884
Independent reflections	3527 [R_{int} = 0.0466, R_{sigma} = 0.0359]	3828 [R_{int} = 0.0277, R_{sigma} = 0.0315]	3811 [R_{int} = 0.0609, R_{sigma} = 0.0245]
Data/restraints/parameters	3527/0/226	3828/0/235	3811/0/245
Goodness-of-fit on F^2	1.039	1.058	1.085
Final R indexes [I>=2σ (I)]	R_1 = 0.0471, wR_2 = 0.1098	R_1 = 0.0308, wR_2 = 0.0659	R_1 = 0.0481, wR_2 = 0. 0963
Final R indexes [all data]	R_1 = 0.0734, wR_2 = 0.1280	R_1 = 0.0404, wR_2 = 0.0711	R_1 = 0.0728, wR_2 = 0.1102
Largest diff. peak/hole / e $Å^{-3}$	0.20/-0.24	0.28/-0.72	0.27/-0.27

Reference

1. W. Kohn, A. D. Becke and R. G. Parr, Density Functional Theory of Electronic Structure, *J. Phys. Chem.*, 1996, **100**, 12974-12980.
2. R. Ditchfield, W. J. Hehre and J. A. Pople, Self-Consistent Molecular-Orbital Methods. IX. An Extended Gaussian-Type Basis for Molecular-Orbital Studies of Organic Molecules, *J. Chem. Phys.*, 1971, **54**, 724-728.
3. Y. Yang, M. N. Weaver and K. M. Merz, Jr., Assessment of the "6-31+G** + LANL2DZ" Mixed Basis Set Coupled with Density Functional Theory Methods and the Effective Core Potential: Prediction of Heats of Formation and Ionization Potentials for First-Row-Transition-Metal Complexes, *J. Phys. Chem. A*, 2009, **113**, 9843-9851.
4. S. Hirata and M. Head-Gordon, Time-dependent density functional theory within the Tamm–Dancoff approximation, *Chem. Phys. Lett.*, 1999, **314**, 291-299.
5. M. Frisch, G. Trucks, H. Schlegel, G. Scuseria, M. Robb, J. Cheeseman, G. Scalmani, V. Barone, B. Mennucci and G. Petersson, Revision D. 01, Gaussian, *Inc., Wallingford CT*, 2009.
6. B. A. Heß, C. M. Marian, U. Wahlgren and O. Gropen, A mean-field spin-orbit method applicable to correlated wavefunctions, *Chem. Phys. Lett.*, 1996, **251**, 365-371.
7. J. Kalinowski, F. Wennmohs and F. Neese, Arbitrary Angular Momentum Electron Repulsion Integrals with Graphical Processing Units: Application to the Resolution of Identity Hartree–Fock Method, *J. Chem. Theory Comput.*, 2017, **13**, 3160-3170.
8. F. J. Avila Ferrer and F. Santoro, Comparison of vertical and adiabatic harmonic approaches for the calculation of the vibrational structure of electronic spectra, *Phys. Chem. Chem. Phys.*, 2012, **14**, 13549-13563.
9. A. Baiardi, J. Bloino and V. Barone, A general time-dependent route to Resonance-Raman spectroscopy including Franck-Condon, Herzberg-Teller and Duschinsky effects, *J. Chem. Phys.*, 2014, **141**, 114108.
10. C. Adamo and D. Jacquemin, The calculations of excited-state properties with Time-Dependent Density Functional Theory, *Chem. Soc. Rev.*, 2013, **42**, 845-856.
11. T. Yanai, D. P. Tew and N. C. Handy, A new hybrid exchange–correlation functional using the Coulomb-attenuating method (CAM-B3LYP), *Chem. Phys. Lett.*, 2004, **393**, 51-57.
12. D. Mester and M. Kállay, Charge-Transfer Excitations within Density Functional Theory: How Accurate Are the Most Recommended Approaches?, *J. Chem. Theory Comput.*, 2022, **18**, 1646-1662.
13. E. D. Hedegård, F. Heiden, S. Knecht, E. Fromager and H. J. A. Jensen, Assessment of charge-transfer excitations with time-dependent, range-separated density functional theory based on long-range MP2 and multiconfigurational self-consistent field wave functions, *J. Chem. Phys.*, 2013, **139**, 184308.
14. E. van Lenthe, J. G. Snijders and E. J. Baerends, The zero-order regular approximation for relativistic effects: The effect of spin–orbit coupling in closed shell molecules, *J. Chem. Phys.*, 1996, **105**, 6505-6516.
15. S. Kossmann and F. Neese, Efficient Structure Optimization with Second-Order Many-Body Perturbation Theory: The RIJCOSX-MP2 Method, *J. Chem. Theory Comput.*, 2010, **6**, 2325-2338.
16. F. Neese, Software update: The ORCA program system—Version 5.0, *Wiley Interdisciplinary Reviews: Computational Molecular Science*, 2022, **12**, e1606.
17. J. Cerezo and F. Santoro, FCclasses3: Vibrationally-resolved spectra simulated at the edge of the harmonic approximation, *J. Comput. Chem.*, 2023, **44**, 626-643.
18. B. Mennucci, Polarizable continuum model, *Wiley Interdiscip. Rev. Comput. Mol. Sci.*, 2012, **2**, 386-404.
19. L. W. Chung, W. M. C. Sameera, R. Ramozzi, A. J. Page, M. Hatanaka, G. P. Petrova, T. V. Harris, X. Li, Z. Ke, F. Liu, H.-B. Li, L. Ding and K. Morokuma, The ONIOM Method and Its Applications, *Chem. Rev.*, 2015, **115**, 5678-5796.

20. A. K. Rappe, C. J. Casewit, K. S. Colwell, W. A. Goddard, III and W. M. Skiff, UFF, a full periodic table force field for molecular mechanics and molecular dynamics simulations, *J. Am. Chem. Soc.*, 1992, **114**, 10024-10035.
21. W. Stauffer, H. Sheng and H. N. Lim, EzColocalization: An ImageJ plugin for visualizing and measuring colocalization in cells and organisms, *Sci. Rep.*, 2018, **8**, 15764.